

A new understanding of the Gemini-Monoceros X-ray enhancement from discoveries with eROSITA

J. R. Knies¹, M. Sasaki¹ , W. Becker^{2,3} , T. Liu² , G. Ponti^{2,4} , and P. P. Plucinsky⁵ 

¹ Dr. Karl Remeis Observatory and ECAP, Universität Erlangen-Nürnberg, Sternwartstraße 7, D-96049 Bamberg, Germany

² Max-Planck-Institut für extraterrestrische Physik, Gießenbachstraße 1, D-85748 Garching, Germany

³ Max-Planck-Institut für Radioastronomie, Auf dem Hügel 69, 53121 Bonn, Germany,

⁴ INAF-Osservatorio Astronomico di Brera, Via E. Bianchi, 46, 23807 Merate (LC), Italy

⁵ Harvard-Smithsonian Center for Astrophysics, 60 Garden Street, Cambridge, MA 02138 USA

Submitted to A&A - under revision, January 2024

ABSTRACT

Aims. The Gemini-Monoceros X-ray enhancement is a rich field for studying diffuse X-ray emission and supernova remnants (SNRs). Most SNRs in this part of the sky are notoriously difficult to observe due to their large extent. With the launch of the extended ROentgen Survey with an Imaging Telescope Array (eROSITA) onboard the Spektrum-Röntgen-Gamma (SRG) platform in 2019, we are now able to fully study those objects for the first time with CCD resolution. Many of the SNRs in the vicinity are suspected to be very old remnants, which are severely understudied in X-rays due to numerous observational challenges. In addition, identification of new faint large SNRs might help to solve the long-standing discrepancy of observed and expected number of Galactic SNRs.

Methods. We performed a detailed X-ray spectral analysis of the entire Gemini-Monoceros X-ray enhancement and a detailed background analysis of the vicinity, which allowed us to model the background with high precision inside the X-ray enhancement. We also made use of multi-wavelength data to better understand the morphology and to constrain the distances to the different sources. Based on the spectral analysis, we estimated the properties of the sources and calculated a grid of model SNRs to determine the individual SNR properties.

Results. Most of the diffuse plasma of the Monogem Ring SNR is well described by a single non-equilibrium ionization (NEI) component with an average temperature of $kT = 0.14 \pm 0.03$ keV. We obtain an age of $\approx 1.2 \cdot 10^5$ yr - consistent with PSR B0656+14 - for the Monogem Ring and explosion energy typical for a CC supernova (SN). In the south-east, we found evidence for a significant temperature enhancement and a second plasma component. Our findings show that a scenario of two SNRs at ≈ 300 pc is likely, with the new candidate having an age of $\approx 50,000$ yr. We were also able to improve on previous results for the Monoceros Loop and PKS 0646+06 SNRs by disentangling the foreground diffuse emission of the Monogem Ring SNR. We obtained significantly higher temperatures than previous studies, and for PKS 0646+06 a much lower estimated age of the SNR. We also found a new SNR candidate G190.4+12.5 which most likely is located at $D > 1.5$ kpc, expanding into a low density medium at a high distance from the Galactic plane, with an estimated age of 40,000 – 60,000 yr.

Key words. ISM: general – ISM: structure – X-rays: ISM – ISM: supernova remnants – supernovae: individual: Monogem Ring

1. Introduction

The Gemini-Monoceros X-ray enhancement is a field rich in diffuse X-ray sources (Nousek et al. 1981). Several supernova remnants (SNRs) have been found and studied in the past in this field. The first detection of X-rays from the region was already made as early as with rocket-flight missions (Bunner et al. 1973). The most prominent source is perhaps the Monogem Ring, a circular X-ray structure with a very large extent of $\sim 25^\circ$ centered around $(l, b) \sim (200^\circ, 8^\circ)$ (Nousek et al. 1981). The first detailed analysis was performed using the ROSAT all-sky survey, where they found low plasma temperatures of $kT = 0.1 - 0.3$ keV, and - assuming an SNR in the Sedov expansion phase - an explosion energy of $\sim 0.2 \cdot 10^{50}$ erg, and a relatively high age of $\sim 86,000$ yr (Plucinsky et al. 1996). The hypothesis that the Monogem Ring is indeed an old nearby SNR was further established with precise distance measurements to the compact object PSR B0656+14, located close to the approximate center of the SNR at $D \approx 300$ pc (Briskin et al. 2003; Thorsett et al. 2003). Additionally, optical filaments were found, which are possibly associated with the remnant (Weinberger et al. 2006). Towards the Galactic

plane, the SNR's shock appears to interact strongly with colder phases of the interstellar medium (ISM), as shown by far-UV observations by Kim et al. (2007). They also found a ring-like structure in $H\alpha$ anti-correlated with the X-ray emission, which they dubbed the “Gemini $H\alpha$ ring”. In our previous study, we showed that this ring was most likely created by a small cluster of massive stars at $D \approx 300$ pc (Knies 2022). We also studied three regions of the Monogem Ring in X-rays with Suzaku observations, confirming previous results for most parts (Knies et al. 2018). Outside of the Monogem Ring, the pair of two SNRs IC443 and G189.6+03.3 is found, and was recently studied with eROSITA (Camilloni & Becker 2023).

Another large SNR was found inside the Monogem Ring in projection at $(l, b) \sim (205.0^\circ, 0.5^\circ)$ with an extent of $\sim 3.5^\circ$, named the Monoceros Loop or G205.5+0.5 (Leahy et al. 1985). Using Einstein IPC X-ray data, they found an SNR that apparently exploded in a low-density environment, leading to the age of $\sim 30,000$ yr and explosion energy of $\sim 3 \cdot 10^{50}$ erg, despite the large extent. They found a distance of 1.5 kpc to be likely, which also suggests that the remnant is located close to stellar cluster NGC 2244 and the Rosette nebula. Indeed, a radio study by

Xiao & Zhu (2012) found signatures for interactions with the nebula, which further narrows down the distance to the remnant. Nearby, another more distant SNR was found: G206.9+2.3 or PKS 0646+06. Also observed with the Einstein IPC, Leahy (1986) found a very low plasma temperature of only ~ 0.14 keV, and the source to be a distant (3 – 11 kpc) old remnant with an age of $\sim 60,000$ yr. The remnant also appears to be emitting in the GeV energy range (Xiang & Jiang 2021). Earlier radio studies constrained the distance of G206.9+2.3 to 3 – 5 kpc (Graham et al. 1982). However, X-ray studies of the Monoceros Loop, PKS 0646+06, and the Gemini-Monoceros X-ray enhancement so far either lacked spectral resolution at full coverage as for the ROSAT data, or coverage at good spectral resolution as for the Suzaku data.

What the numerous studies of sources inside the Gemini-Monoceros X-ray enhancement showcase is that for studying SNRs, this field is truly a treasure trove. This is especially true for studying the evolution of very old remnants, which is usually very difficult at higher distances due to absorption and low surface brightness. Moreover, these faint large SNRs might contribute to the issue of missing SNRs in our Galaxy, compared with model predictions (e.g. Anderson et al. 2017; Ranasinghe & Leahy 2022). Previous studies in radio discovered many additional SNRs, but still leaving a factor two unaccounted for (Anderson et al. 2017). Therefore, we need high quality all-sky (soft) X-ray data to trace these objects, too faint to be discovered in radio. With the launch of the extended ROentgen Survey with an Imaging Telescope Array (eROSITA) in 2019 and the consequent four all sky surveys (eRASS), we now have the unique opportunity to again study this rich field with unparalleled spectral resolution and coverage (Predehl et al. 2021).

Our paper is divided into the following sections: In Sect. 2 we introduce the data we used and in Sect. 3 we explain the X-ray data reduction procedure. The X-ray and multi-wavelength morphology is discussed in Sect. 4, the background analysis and X-ray spectral model are discussed in Sect. 5. In Sect. 6 we present the spectral analysis of the SNRs, in Sect. 7 we discuss the implications from our results of the spectral analysis and morphology, and compare our findings to SNR model calculations. Finally, in Sect. 8 we summarize our work.

2. Data

2.1. X-ray

We used X-ray data obtained with eROSITA, launched in July 2019 as part of the Spectrum-Roentgen-Gamma (SRG) mission (Predehl et al. 2021). The data were observed from January 2020 to December 2021 during the first four all-sky surveys (eRASS 1-4, the total also called eRASS:4, Merloni et al. 2023). The data cover the energy range of ~ 0.2 –10 keV with an energy resolution of ~ 80 eV at 1.49 keV, and a field of view (FoV) averaged spatial resolution of $\sim 26''$. We used the data processed with the 020 pipeline version, which has improved calibration, especially at lower energies, compared to previous processing versions. For the data reduction and analysis, we used the eSASS software¹ version eSASSuser2112104 (Brunner et al. 2022) with the most recent (2021Q4) calibration database available at the time of the data reduction (CaLDB, Brunner et al. 2018).

¹ <https://erosita.mpe.mpg.de/edr/DataAnalysis/>

2.2. Optical

To compare the X-ray emission with other wavelengths, we used the H α maps by Finkbeiner (2003) that cover most of our field with a resolution of $6'$. The map was created by combining the Virginia Tech Spectral line Survey (VTSS, Dennison et al. 1998), Southern H-Alpha Sky Survey (SHASSA, Gaustad et al. 2001), and the Wisconsin H-Alpha Mapper (WHAM, Reynolds et al. 2002).

We also used the dust absorption A_V data cubes obtained by Lallement et al. (2022). The data cubes map the interstellar absorption in 3D in a $6 \text{ kpc} \times 6 \text{ kpc} \times 0.8 \text{ kpc}$ volume around the Sun, derived from the Gaia EDR3 and 2MASS photometric data.

2.3. Radio and sub-mm

To trace the cold ISM, we also used data cubes derived from HI measurements by (Clark & Hensley 2019), which include the Stokes I, Q, and U moment maps. The original data were obtained by the HI4PI 21 cm neutral hydrogen (HI) survey (HI4PI Collaboration et al. 2016).

We also made use of τ_{353} Planck total intensity data at 353 GHz (Planck Collaboration et al. 2020). The data have a resolution of $\sim 5'$ and were released as part of the Planck legacy release 3.

3. X-ray data analysis

3.1. Images

We first merged all events of the sky tiles covering the Gemini-Monoceros X-ray enhancement and its vicinity. All available data from eRASS1 to eRASS4 were used (eRASS:4 hereafter) using `evttool`. In total 160 sky tiles were used. During merging, we applied the strict flag `0xc00f7f30` to remove bad events². We also manually applied a good time-interval (GTI) filtering to remove a narrow stripe across the field with strongly enhanced background - likely due to solar flaring - between the times $6.87312 \cdot 10^8$ s and $6.87357 \cdot 10^8$ s (MJD). We accepted all event patterns from singles to quads with `pattern = 15`.

There are also bad pixels, which are not in the calibration database (CaLDB) that have limited impact or are limited to certain specific times. We manually filtered out the events on these pixels to reduce any possible contamination. Only $\sim 0.3\%$ of events were selected by this filtering. Since our sources of interest are very faint compared to the background, we further investigated the effects by creating images with and without filtering, and compared those. The filtered pixels appear uniformly distributed across the Monogem Ring SNR, with enhancements following the real X-ray emission. Therefore, real events were also filtered out by this procedure, while suspicious structures like stripes in the scanning direction suggesting a time variable effect of the detectors were not found. Therefore we decided to keep those events. Internal tests performed by the eROSITA team showed that contamination by those pixels were constrained in very small stripe-like regions over the sky, showing no spatial overlap with our data³.

Next, we created images for three different energy bands with `evttool`: 0.2-0.4, 0.4-0.8, and 0.8-1.25 keV. These soft bands were chosen to highlight differences in the relatively soft X-ray emission in the field. We also created exposure maps for each of

² https://erosita.mpe.mpg.de/edr/DataAnalysis/prod_descript/EventFiles_edr.html#First_Sub_Point_312

³ Private communication, Michael Yeung

the bands by using `expmap`. The exposure time of the data across the analyzed field after filtering is on average 337 ± 77 s (1σ). Finally, we created exposure-corrected images by dividing the images by the exposure map and removing artifacts from pixel values below zero.

3.2. Point-source removal

In order to reduce the contamination from point sources, we used the internal combined eRASS:4 point source catalog to obtain a list of point source candidates. The detection criteria were similar to the eRASS1 catalog, which will be published with the first eROSITA data release (3B in Merloni et al. 2023). We filtered the catalog with a minimum detection likelihood of 20 in the full 0.2 – 5.0 keV energy band. For each point source candidate, we used a fairly large fixed radius of $46''$ to fully remove contaminating emission. In a second step, we carefully checked by hand if any additional contamination was still left, after applying a cheese mask based on the point source list. As a result, several extended fore-/background sources, where the fixed radius was inappropriate, as well as missed point-like sources, were excluded to minimize possible contamination of other sources.

3.3. Spectra

We extracted spectra as well as response files for each analysis region using `srctool`. We used the combined, filtered eRASS:4 eventfile, additionally applying the FLAREGTI GTI filtering. For the response files, we assumed the point-spread function (PSF) to be a delta function, and a top-hat profile with an initial extend value equal to the approximate radius of the region for the source emission. The accuracy of the response file sampling was chosen as $2'$ for the statistically derived region, and varying appropriate sampling size for manually defined regions. Due to the large region sizes used in our analysis, the coarser sampling did not impact the quality of the spectra, while significantly reducing computation times. For the extraction of the events in the respective region we created and applied masks. Point-source candidates have been also excluded with these masks, as described above. We did not subtract background spectra from the source, instead we extracted background spectra in the vicinity of the Monogem Ring, as explained in detail below.

4. Morphology

X-rays: The three-color large-scale image of the Gemini-Monoceros X-ray enhancement shown in Fig. 1 reveals a highly complex structure of the diffuse emission. To the east (left-handed) side we observe a half ring-like emission with a radius of $\sim 10^\circ$ (Green Arc, Fig. 2). The emission appears to be harder towards to south-east (i.e., more green), with the softer (red) emission more pronounced towards the center and north. The green emission appears almost ring-like, while the red emission seems to have a more complex morphology. To the west (right) we observe a very soft emission with a broken-up structure in most parts (broken up soft ring, Fig. 2). The center of the diffuse emission is significantly darker, which could indicate limb-brightening of the deformed expanding shell of the SNR. We measure an increase in brightness by 50% when comparing the darkest central region with the shell. In the south-west, we find the more distant Monoceros Loop and PKS 0646+06 SNRs as shown in Fig. 3, accompanied by harder X-ray emission compared to the surroundings (grey and blue circle, Fig. 2). The soft (red) emission of the

Monogem Ring SNR and the more distant SNRs appear to be overlapping in projection. Towards the north, we observe an almost perfect circular diffuse emission structure, only visible in the medium band (G190.4+12.5 hereafter, Fig. 2).

H α : An overlay between X-ray image and H α contours are shown in Fig. 4. Towards the Galactic Plane (right), we observe strong H α emission with a complex morphology. The Gemini H α ring is located towards the north in the H α emission (Kim et al. 2007). This structure appears to be almost perfectly anti-correlated with the soft X-ray emission. The Gemini H α ring (white dashed ring, Fig. 4) is believed to be interacting with the Monogem Ring SNR and caused by massive stars, which existed at similar distances as the Monogem Ring SNR, as shown in our previous studies (Knies et al. 2018; Knies 2022) and the UV study by Kim et al. (2007). The H α emission towards the south and west appears to be slightly weaker while also not showing any clear (anti-)correlation with the X-rays. Therefore, these parts of the H α emission are most likely unrelated with the diffuse X-ray emission.

Dust: From the A_v 3D cubes by Lallement et al. (2022) we created contours, which we overlay on the soft X-ray emission in Fig. 5. We integrated the cube along the line of sight for three distance slices ranging from 300 to 1120 pc. We also integrated below 300 pc but observed no interesting feature.

In the distance slice 300–600 pc we observe a small overlap in the south without any clear anti-correlation with X-rays. In the next slice 600 – 900 pc we find an interesting absorption feature right in the center of the remnant, which almost perfectly matches a depression in X-ray intensity (edge of green emission, Fig. 2). Also in the south towards the Galactic plane, there appears to be a significant absorption, however, here we do not observe any anti-correlation with X-rays. In the last slice 900 – 1120 pc, we observe no (anti-)correlation whatsoever, despite significant A_v absorption in the lower half of the shown frame. An in-depth discussion of the implications is given in Sect. 7.2.

τ_{353} : We show the comparison between X-rays and τ_{353} - the thermal dust emission at 353 GHz - in Fig. 6. The sub-mm dust contours are consistent with the dust contours derived from optical data shown in Fig. 5. Interestingly, the lowest contour level also traces the edge of the green diffuse emission in X-rays well on large scales. The contours also confirm the central absorption feature that we see in Fig. 5, albeit the exact shape depends on the chosen contour levels.

5. Study of the astrophysical X-ray background

5.1. Aim

Estimating an appropriate X-ray background for diffuse sources can be challenging. This is especially true for large extended objects and regions in the sky, like the Gemini Monoceros X-ray enhancement, subject of this study. The background may vary spatially to a great extent over the entire object. Therefore, in preparation of the X-ray spectral analysis, we performed an extensive study of the background emission. Usually, a region close to the object with little to no emission from the actual object itself is an appropriate choice to extract the background emission. However, since the diffuse emission of our region extends over several degrees, it makes this approach unfeasible.

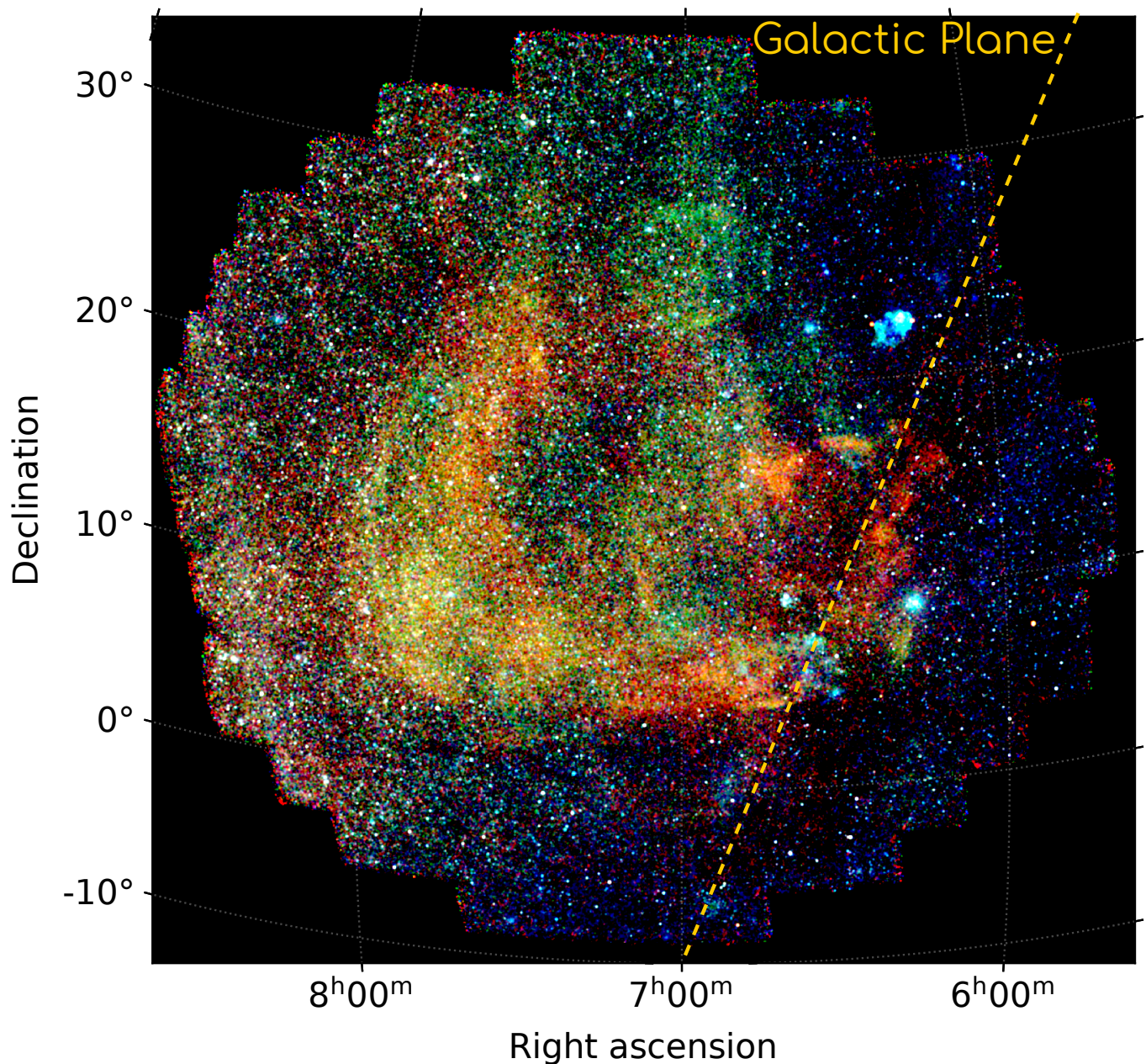


Fig. 1: eROSITA X-ray three-color image of the Gemini-Monoceros X-ray enhancement with the energy bands: 0.2-0.4 keV (red), 0.4-0.8 keV (green), and 0.8-1.25 keV (blue). The image was created from the combined eRASS:4 data.

Instead, we defined regions surrounding the entire X-ray enhancement, where no emission from the source is visible anymore. The regions are shown in Fig. 7 and were optimized by hand over several iterations. Too large regions resulted in unreliable average values due to strong variations within the extent of one region, while too small regions did not have sufficient statistics for a precise spectral analysis. Additionally, we avoided regions in the sky that clearly showed diffuse emission from fore- and background sources. Since the spatial distance between the source regions and the background can be quite large, we performed a more in-depth study of the background. The aim was to create an accurate X-ray model of the Galactic- and instrumental background for each given coordinate inside the large extended source.

5.2. Spectral analysis

5.2.1. Model

For our spectral analysis of the background, we used the individual spectra of detectors TM1 – 4 and TM6. We account for the following Galactic components in our model: the local hot bubble (LHB), the circumgalactic medium (CGM) and the hot Galactic corona.

The local hot bubble is a component visible over the entire sky, which can be described as emission from a thermal plasma with a temperature $kT \sim 0.1$ keV (Yeung et al. 2023). As shown by Liu et al. (2017) there are slight variations in the temperature and emission strength for different parts of the sky, with the peak temperature close to $kT = 0.1$ keV. We used the `APEC` model (Smith et al. 2001) to describe the LHB, constraining the

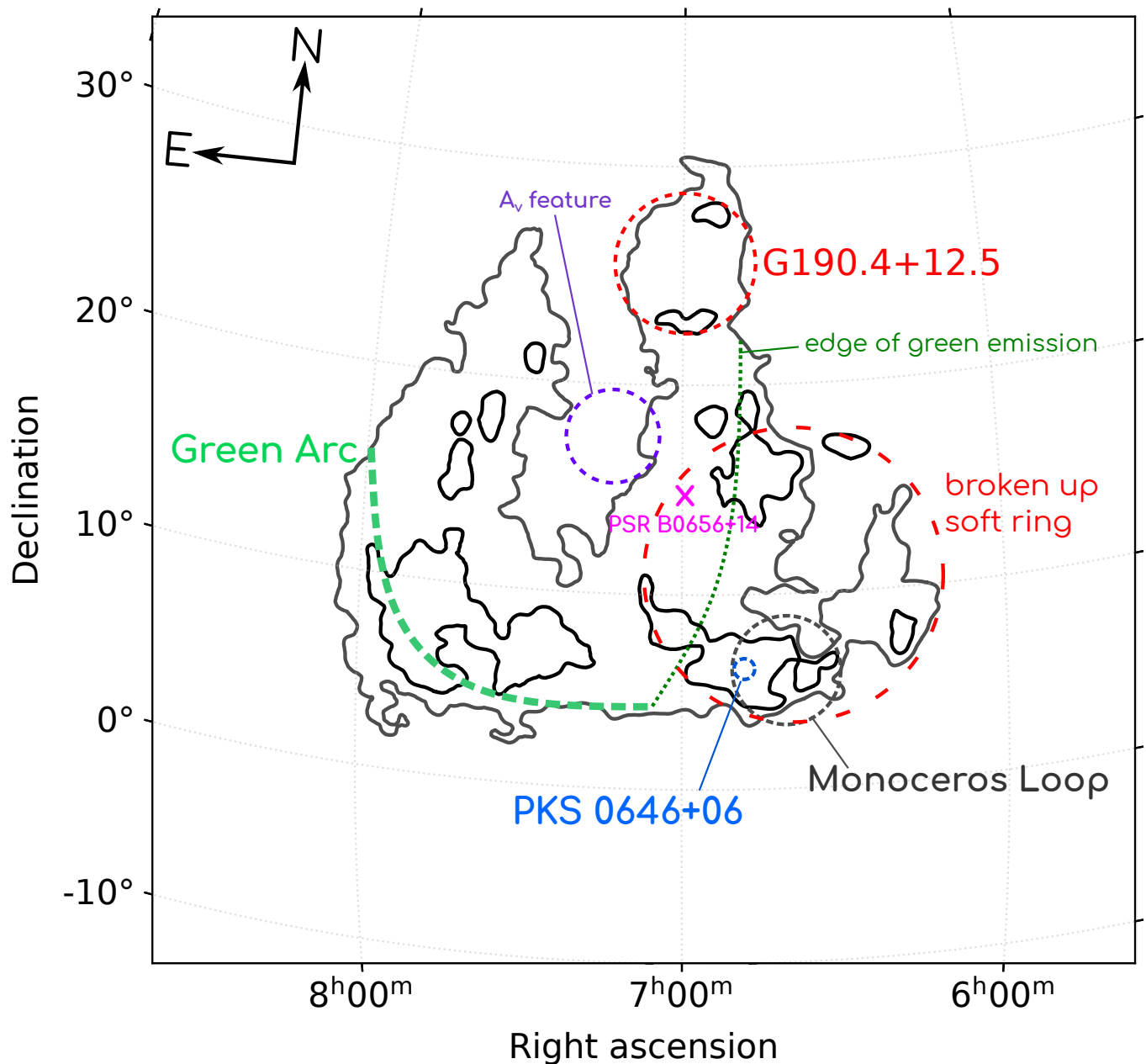


Fig. 2: X-ray finding chart based on the eROSITA data in the 0.2-1.25 keV energy range, showing the same frame as Fig. 1. Prominent sources and regions mentioned in the text are highlighted for better orientation.

temperature to $kT = 0.09 - 0.12$ keV with solar abundances, with the range constrained to the results shown in Fig. 6 in Liu et al. (2017). The normalization was let free to fit and later compared to the emission measure (EM) reported in their work.

Next, we introduced an absorption component (TBABS) to account for Galactic absorption along the line of sight. We fixed the value to the column density of the HI4PI survey value (HI4PI Collaboration et al. 2016) at the respective positions of the extracted spectra and multiplied this component with the following Galactic components. The second Galactic component describes the circumgalactic medium, now believed to be an intrinsic property of galaxies (Fukugita & Peebles 2006). We also used the thermal APEC model for this component. The temperature of this component is believed to be close to the virial temperature $kT = 0.15 - 0.25$ keV (Gupta et al. 2021; Ponti et al. 2022),

while the exact structure and distribution is still not fully understood. Previous studies have shown that the chemical abundances of this component are significantly sub-solar in the range from $\sim 0.05 - 0.3 Z_{\odot}$ (e.g., Fukugita & Peebles 2006; Bregman et al. 2018; Ponti et al. 2022). We initially let this parameter free to fit and then fixed it to the median of the best fit value over all regions, as we proceeded with the analysis. This was done to account for the relatively low statistics, which led to the parameter not being well constrained, as our uncertainty calculations showed. We obtained a median of $Z \sim 0.11 Z_{\odot}$ for the abundance, which appears consistent with the low values obtained by Ponti et al. (2022).

The third Galactic component accounts for emission from a hotter Galactic component, which might also be part of the CGM and could be caused by unresolved sources in the Galactic disk.

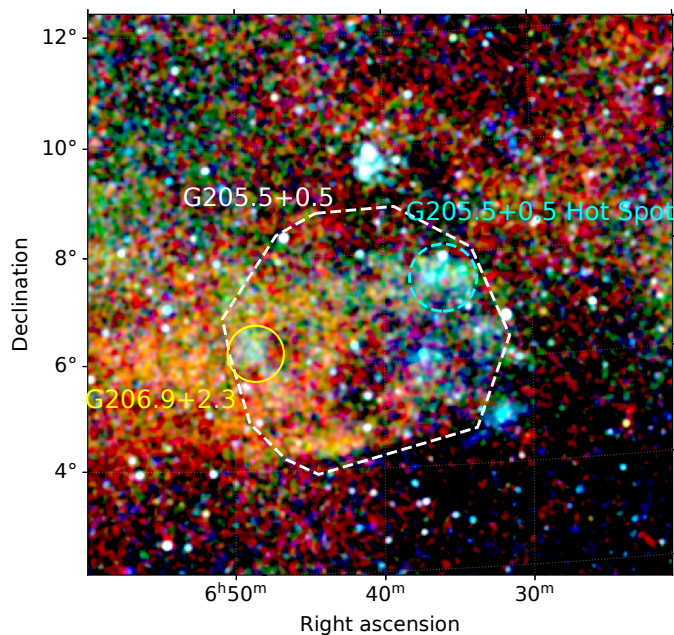


Fig. 3: A detailed view of the vicinity of G205+0.5 (Monoceros Loop SNR), with the same energy bands and data as in Fig. 1. The extent of the Monoceros Loop is shown with a white dashed region, while the hot spot is shown in cyan. PKS 0646+06 (G206.9+2.3) is shown in yellow (Green 2019).

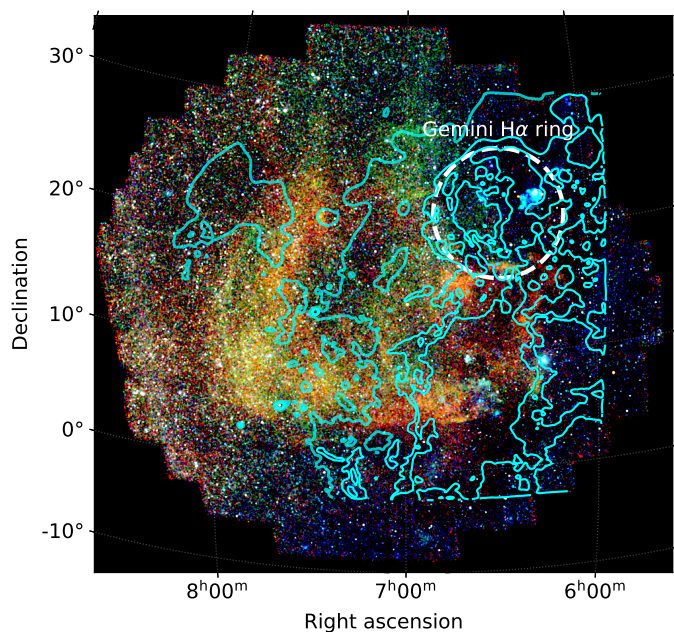


Fig. 4: Three-color X-ray mosaic as in Fig. 1 with $H\alpha$ contours overlaid in cyan (Finkbeiner 2003). The lowest contour level has a lower transparency for better visibility. The contour levels are 3.86, 8.11, and 12.35 Rayleighs, corresponding to the 40%-82.5% percentiles of the $H\alpha$ image.

Previous studies have suggested a temperature $kT > 0.6$ keV, and therefore significantly hotter than the CGM, with a thermal nature (e.g., Yoshino et al. 2009; Gupta et al. 2021; Ponti et al. 2022; Locatelli et al. 2023). Therefore, we again used the $APEC$ model. We initially let the temperature free to fit, but similar to

the CGM abundance, the uncertainties on the temperature was large. Therefore, we fixed the value to the median best-fit value of $kT \sim 0.7$ keV, which is in good agreement with the previously mentioned studies. The abundances were fixed to solar values.

To describe the extra-galactic background (CXB), we used a double broken-powerlaw. The CXB was also multiplied with the $TBABS$ Galactic absorption component. The indices were defined as $\Gamma_1 = 1.96$ for $E < 0.6$ keV, $\Gamma_2 = 1.75$ for $0.6 < E < 1.2$ keV, $\Gamma_3 = 1.45$ for $E > 1.2$ keV. This model was shown to yield an accurate description of the background also down to lower energies (Gilli et al. 2007). The model includes the small modification for eROSITA used by Ponti et al. (2022) to account for residuals at lower energies that were present without the modification ("CXBs" in Ponti et al. 2022). This model performed slightly better in our case compared to the canonical model ("CXB") in their study. We set the initial normalization to $7.7 \cdot 10^{-7}$ photons/keV/cm²/s which is equal to ≈ 8.3 photons s⁻¹ cm⁻² sr⁻¹. After the initial fit, the normalization is set free to fit.

The extraction areas A of the respective spectra are taken into account with a normalization constant, set to the exact area in arcmin². This also has the benefit of making the normalization between different regions and detectors comparable.

We also considered possible contamination by solar wind charge exchange (SWCX). For this, we introduced an unabsorbed "AtomDB Charge Exchange Model v2.0" (ACX2, Smith et al. 2012; Foster et al. 2020)⁴ (v1.1.0) component to our spectral model described in Eq. 1. This model takes into account the complex charge exchange reactions based on atomic data. We used the model by fixing the temperature to the typical temperature of $kT = 0.1$ keV in the initial fit (Smith et al. 2012) and then constraining the temperature to $kT = 0.07 - 0.13$ in the second iteration. The study by Ponti et al. (2022) yielded a slightly higher temperature of $kT = 0.136 \pm 0.007$ keV, however, if we left the temperature completely free to fit, most best-fit values centered around $kT \approx 0.1$ keV. A possible cause might be the different ecliptic latitude of our background regions as well as different times and therefore solar activities when the data were taken. The collision parameter, equal to the wind velocity, was fixed to 450 km/s, typical for the slow solar wind (Cumbee et al. 2018). This velocity appears to also be appropriate as a mean solar wind velocity (Zhang et al. 2022). We also tried to let this parameter free, however, it was poorly constrained while not improving the fit. We only considered a single recombination for the calculation of the spectrum, as expected for SWCX.

In addition, we account for inter-detector calibration differences with a constant free to fit close to unity in the range 0.75 – 1.25 (CAL). In summary, we used the following model expression in `xspec`:

$$\text{CONSTANT}_{\text{CAL}} \times \text{CONSTANT}_A \times (\text{ACX2} + \text{APEC}_{\text{LHB}} + \text{TBABS} \times (\text{APEC}_{\text{CGM}} + \text{APEC}_{\text{Corona}} + \text{BKN2POW}_{\text{CXB}})) \quad (1)$$

The second part of our model accounts for the non-X-ray background which can be studied using the data taken with the filter-wheel closed (FWC). We adopted the model based on a detailed study of the FWC data by Yeung et al. (2023). The FWC data were taken by eROSITA during calibration and service intervals. The phenomenological model describes the FWC background for each individual detector with high precision. Since this background does not conform to the regular photon paths, this model was only folded with the Redistribution Matrix File

⁴ <https://github.com/AtomDB/ACX2>

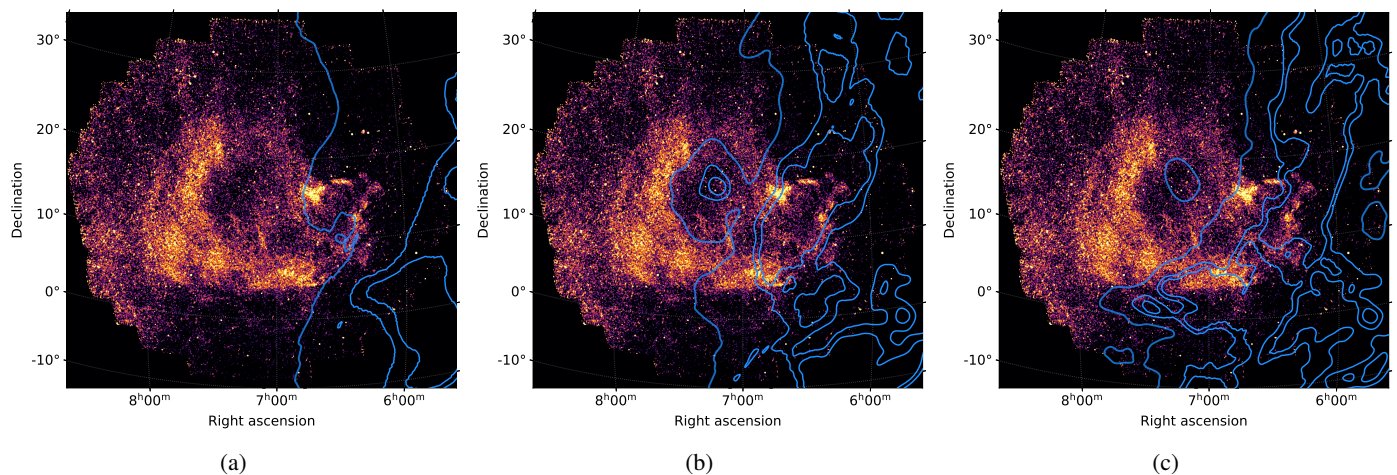


Fig. 5: Soft X-ray image in the energy range 0.2–0.4 keV, overlaid with distance-integrated slices of the A_v absorption derived by Lallement et al. (2022). The images show A_v contours for 300–600 pc (a), 600–900 pc (b), and 900–1120 pc (c). The contours correspond to the 65%–95% percentiles of the A_v data, linearly spaced.

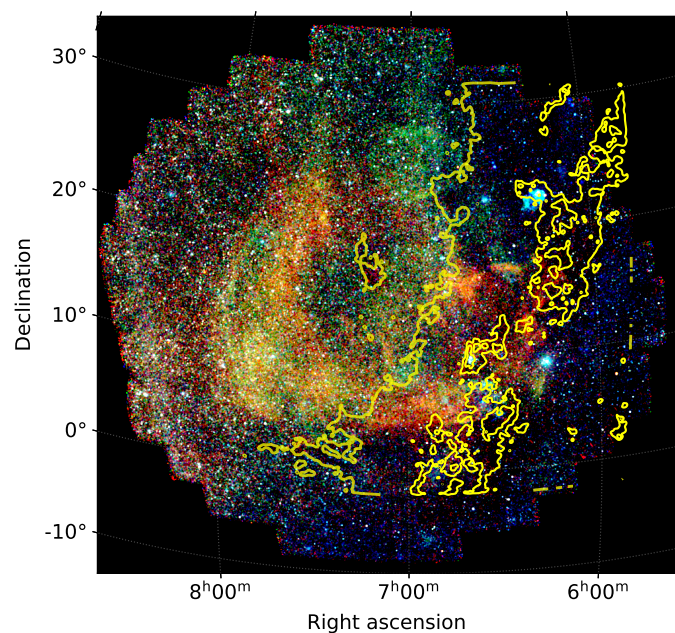


Fig. 6: Three-color X-ray mosaic as in Fig. 1 with Planck τ_{353} contours overlaid in yellow (Planck Collaboration et al. 2020). The lowest contour level has a lower transparency for better visibility. The contour levels are 0.0025, 0.0126, and 0.0227 K, corresponding to the 50%–99% percentiles of the τ_{353} data.

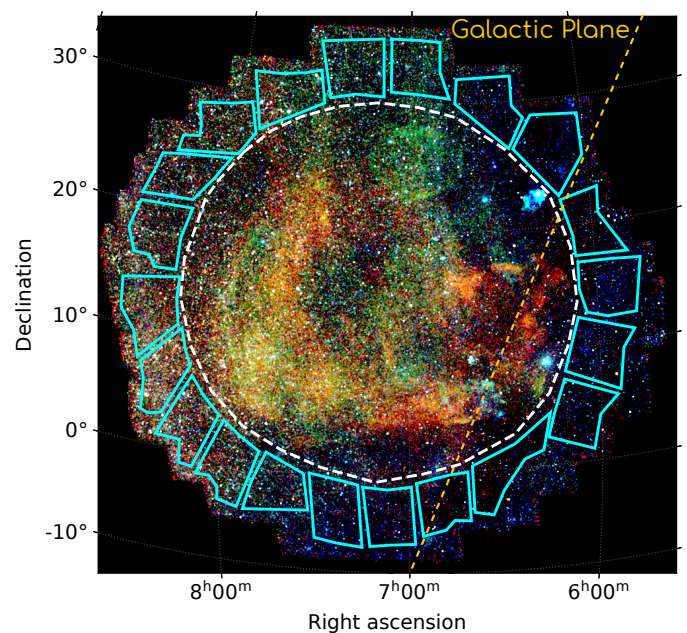


Fig. 7: eROSITA X-ray image (Fig. 1) with the regions defined for the background analysis shown in cyan, as well as the Galactic plane in yellow.

5.2.2. Spectral fit

In all our spectral fits presented in this paper, we used the cash statistic (cstat, Cash 1979) on unbinned spectra to optimize the use of the sparse X-ray data. We will use the metric $\text{cstat}/\text{d.o.f.}$ to assess our spectral fits in the following, since it leads to more accessible numbers than the absolute cstat value. While strictly speaking the $\text{cstat}/\text{d.o.f.}$ is not directly comparable to the typical $\chi^2/\text{d.o.f.}$, since we use roughly always the same d.o.f. for our background fits, and within the spectral analysis later, this quantity is still very useful for comparing the quality of the fits. For most contour-bins, background regions, and manually defined regions, we have enough counts to safely use $\text{cstat}/\text{d.o.f.}$ as a goodness-of-fit quantity (Kaastra 2017).

(RMF), but not the Auxiliary Response File (ARF). We added a normalization constant to the FWC model to account for differently sized true detector extraction region compared to the original FWC data. A detailed definition of the model is given in Appendix B in Yeung et al. (2023). We will refer to the entire model as “Model B” hereafter. An alternative model (“Model A”) is also described in Appendix B. For all models and spectral fits in this work, we used the elemental abundances of *wilm* (Wilms et al. 2000).

For the spectral fit of the individual regions, we first estimated the normalization of the FWC model. We only used the data in the hard energy tail of the spectra in the $E = 3.0 - 9.0$ keV range, where the FWC emission dominates the spectrum. The normalizations for the different TM FWC models were independent from each other, and completely free to fit. We then performed a fit and calculated the uncertainties, using the `ERROR` command. The normalization constants were then constrained to the calculated uncertainty range and set to the best-fit value.

Next, to model the X-ray background, we considered the data in the energy range of $E = 0.2 - 3.0$ keV for TM1, TM2, and TM6, and $E = 0.25 - 3.0$ keV for TM2 and TM4. We fixed the detector normalization constant (CAL) of TM1 to unity, while we constrained the other constants individually to the aforementioned range. The second constant in the model was fixed to the extraction sky-area A in arcmin² and linked between different TMs. All other parameters of the X-ray model were linked between detectors to reduce the number of free parameters, under the assumption that any calibration difference is accounted for with the first constant. For the LHB component, we set the initial temperature to $kT = 0.1$ keV, while the CGM temperature was set to $kT = 0.16$ keV, free to fit in the range $kT = 0.15 - 0.25$ keV. As previously mentioned, the corona component had a fixed $kT = 0.7$ keV. For all APEC components, we set an initial normalization of $\eta = 10^{-6}$ cm⁻⁵ in XSPEC but completely free to fit. The CXB broken-powerlaw normalization was initially frozen to $\eta = 7.7 \cdot 10^{-7}$ photons/keV/cm² which equals ≈ 8.3 photons s⁻¹ cm⁻² sr⁻¹. After an initial fit, the CXB normalization was let free to fit in the second iteration.

After the final fit, we performed an uncertainty calculation on the relevant background fit parameters.

5.3. Results

With ‘‘Model B’’ as described above, we obtained very good fit statistics for all regions, as shown in Fig. 9a. The average reduced fit statistic and standard deviation is $\text{cstat/d.o.f.} = 1.08 \pm 0.05$. An example of two spectra, one close to the Galactic plane at $b \sim 3.6^\circ$ and another far from the Galactic plane at $b \sim 22.1^\circ$, are shown in Fig. 8a and Fig. 8b, respectively, and the different model components are indicated.

In the following we discuss the individual components. The most important fit parameters of the individual components are shown in Fig. 9. The respective median values were calculated from the best-fit values, while the lower and upper limits shown in the diagrams are equal to the median lower and upper uncertainties. The respective values are shown along the Galactic latitude of the associated background regions. The normalization of the LHB component (Fig. 9b) appears to be very consistent across all background regions, yielding a median of $\eta_{\text{LHB}} = 1.03^{+0.10}_{-0.12} \cdot 10^{-6}$ cm⁻⁵ arcmin⁻². We see a small increase in the normalization for some regions at higher longitudes (triangle up), but considering the uncertainties, they are only slightly outside the expected statistical scatter. We compared our median normalization η with the LHB study by Liu et al. (2017) by converting it to an emission measurement (EM). The APEC normalization is defined as

$$\eta = \frac{10^{-14}}{4\pi D^2} \int n_e n_H dV [\text{cm}^{-5}], \quad (2)$$

where n_e and n_H are the electron and hydrogen densities, respectively, and D the distance to the source. If we only consider the

area in the line of sight, this can be expressed as

$$\eta = 10^{-14} \frac{\theta}{4\pi} \int n_e n_H dl, \quad (3)$$

where θ is the emission area in the sky in units sr (Ponti et al. 2022). Since we normalized the models to arcmin², this yields $\theta = (1/60 \cdot \pi/180)^2$. With this, we obtain

$$\text{EM} = \frac{\eta}{2.081 \cdot 10^{-4}} [\text{cm}^{-6} \text{pc}]. \quad (4)$$

Using Eq. 4 we obtain an emission measure of $\text{EM} = (4.95^{+0.48}_{-0.58}) \cdot 10^{-3} \text{cm}^{-6} \text{pc}$ which is consistent with the measurements by Liu et al. (2017) at the position of the Monogem Ring, within uncertainties.

The CGM results are shown in Fig. 9c and Fig. 9d. We obtained relatively uniform temperatures around the median value of $kT \sim 0.18$ keV for the majority of the regions, where some show higher temperatures up to 0.25 keV, albeit with relatively large uncertainties in most cases. The normalization of the CGM appears strongly enhanced for background spectra obtained near the Galactic disk ($\pm 5^\circ$). If we exclude the outlier near $\sim 0^\circ$, the increase is up to a factor of ~ 5 around the disk, compared to the median value $\eta_{\text{CGM}} = 1.30^{+0.17}_{-0.19} \cdot 10^{-5}$ cm⁻⁵ arcmin⁻².

For the hot corona, we also obtained a strong dependence on the Galactic latitude for the normalization, as shown in Fig. 9e. The median of the normalization is $\eta_{\text{Corona}} = 2.45^{+0.27}_{-0.28} \cdot 10^{-7}$ cm⁻⁵ arcmin⁻². In comparison to the CGM, this component’s normalization is smaller by two orders of magnitude. One possible origin of the hot corona component are stars, and especially dwarf M star spectra show a remarkably similar temperature to this component (Giampapa et al. 1996; Wulf et al. 2019). Since the population should roughly correlate with the mass profile of the Milky way, we compared model predictions to our results (solid lines, Fig. 9e). The models are based on the theoretical predictions by Bienayme et al. (1987) and McMillan (2017), reprojected onto the average galactic longitude of the Gemini-Monoceros X-ray enhancement. While the normalizations of the profiles are arbitrary, we obtain a surprisingly good agreement between the profile shape of the predicted mass profile denoted ‘‘Bienayme’’ and the hot corona normalization. This result indicates that indeed this component could be caused, at least partially, by the stellar population. In addition, our results for the hot corona show, that we are indeed fitting a physical component of the Milky way.

For the extragalactic background, we obtain a median normalization of $\eta_{\text{CXB}} = 9.66^{+0.19}_{-0.20} \cdot 10^{-7}$ photons/keV/cm² arcmin². We obtain a few outliers outside the expected statistical scattering with values lower or higher by about $\sim 10\%$, which might be caused by local enhancements in the background. Compared to previous studies, our values are slightly higher by about $\sim 10\%$ (Kuntz & Snowden 2000; Snowden et al. 2008). This might be caused by our very high number of point-source candidates removed from the spectra. Since removing point sources effectively changes the slope of the CXB, the higher normalization compensates the fixed power law indices in our model.

We also tried an alternative description of the background by decoupling the CGM and hot halo component absorption. The results are discussed in Appendix B. However, this alternative model was not chosen for the following spectral analysis due to inconsistencies of the description of the SWCX contamination.

5.4. Application to the spectral analysis

From our results it is clear that there is a strong variation over Galactic latitude of the background, and to a lesser degree also

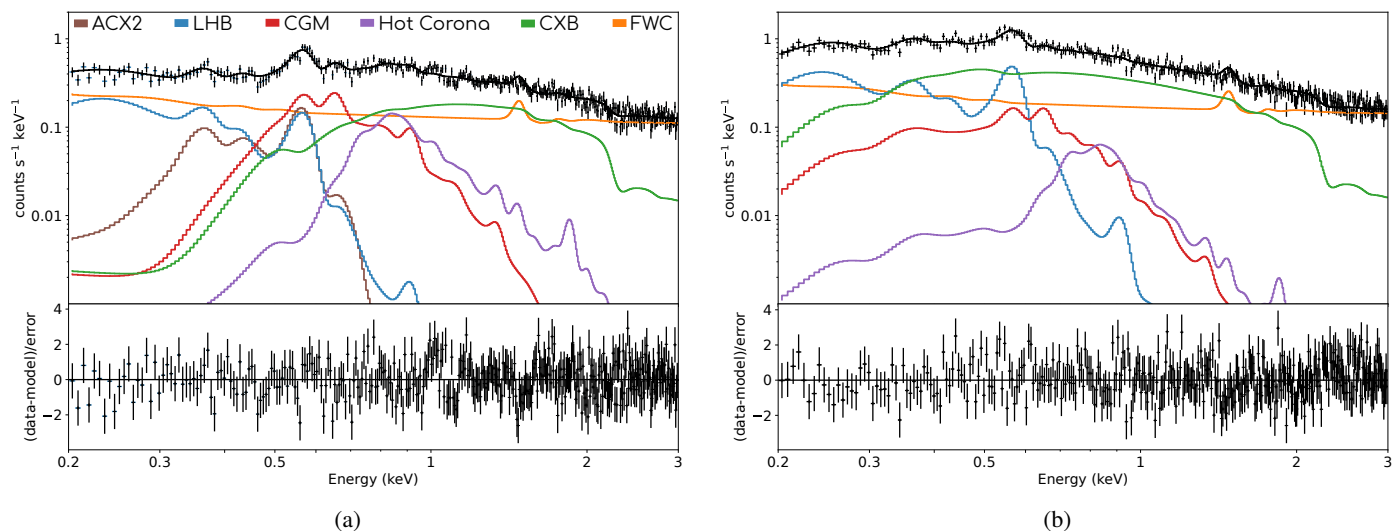


Fig. 8: Background spectrum and fitted model near the Galactic plane at $b \sim 3.6^\circ$ (a) and out of the plane at $b \sim 22.1^\circ$ (b). The data and total best-fit model are shown in black and the different model components are shown with the colors according to the legend in (a). For visual purposes only, the spectra were binned with a minimum 5σ or 50 counts per bin and for better visibility only the spectrum and model for TM1 is shown.

over the Galactic longitude. Therefore, in order to apply the results, we need to take into account both the Galactic latitude, as well as the absolute distance between background and source region. One of the benefits of having many different background regions is that we are also able to estimate the background from more than one region. This also helps to cover "gaps" in our coverage, which are the indirect result of our spatial sampling, or simply speaking, of the size, and therefore of the number of the background regions. By averaging several regions, we can easily interpolate between the background samples.

After some initial testing, we obtained good results by using the spectral fit results of the four most appropriate background regions for each source region. From the relevant background spectral fits, we estimated the background parameters for the respective position of the source centroid. The four background regions were selected based on their Galactic latitude being the closest to the source position. To also properly take into account both the Galactic latitude difference and angular distance between the background and source region, we used the weighted average

$$\bar{x} = \frac{\sum_{i=1}^n w_i x_i}{\sum_{i=1}^n w_i}, \quad (5)$$

where the weights are given by

$$1/w_i = 2d_{\text{gal},b,i} + d_{\text{abs},i}, \quad (6)$$

with $d_{\text{gal},b,i}$ and $d_{\text{abs},i}$ being the distance in Galactic latitude and the angular distance between the source and background region centroid positions, respectively. Since the variation along the Galactic latitude is significantly stronger, we weigh this distance with a factor of two, compared to the projected distance. By additionally accounting for the projected distance, we prevent for example background regions from the opposite site of the remnant being weighted higher just because they have a closer Galactic latitudes.

Applying this background estimate, we obtained very good fits for most of the source regions. For a handful of isolated regions, we were able to further improve the fit significantly by

allowing uncertainties larger by a modest 10% of what we obtained from the weighted average. This effect might be caused by local variations in the background that deviate from the interpolated value. We therefore adopted this small modification and increased the uncertainty/fit range after the weighted average calculation by 10% if we obtained a sub-optimal fit ($\text{cstat/d.o.f.} > 2000/1752 = 1.14$) which solved the remaining issues for all source regions.

6. X-ray spectral analysis

6.1. Spectral analysis regions

6.1.1. Manually defined regions

We manually defined spectral analysis regions based on three criteria: the X-ray three-color image in Fig. 1, the $\text{H}\alpha$ emission in Fig. 4, and finally the dust optical depth A_v in the line of sight as shown in Fig. 5. The regions are shown in Fig. 10. We first defined the regions based on the color in the X-ray three-color image, which corresponds to the hardness, to obtain regions with apparently similar spectral properties. In a second step, we optimized those regions by comparing them to the $\text{H}\alpha$ emission. Regions which had vastly different $\text{H}\alpha$ emission gradients were adjusted to better reflect the $\text{H}\alpha$ morphology. In a last step, we compared the regions to the dust map in the range of 600 – 900 pc, where we observe a possible (anti-)correlation. Again, we modified the regions to align with strong gradients, here in the A_v dust absorption.

6.1.2. Contour binning

In addition to the manually defined spectral analysis regions, we also created regions purely based on the statistics of the data. This allows us to systematically cover the entire region while minimizing any observer bias. For this, we implemented the contour-binning method by Sanders (2006). This method allows to specify a certain S/N while also taking into account the shape of the diffuse emission. In our previous works (e.g., Knies et al. 2021; Sasaki et al. 2022) we implemented the Voronoi binning

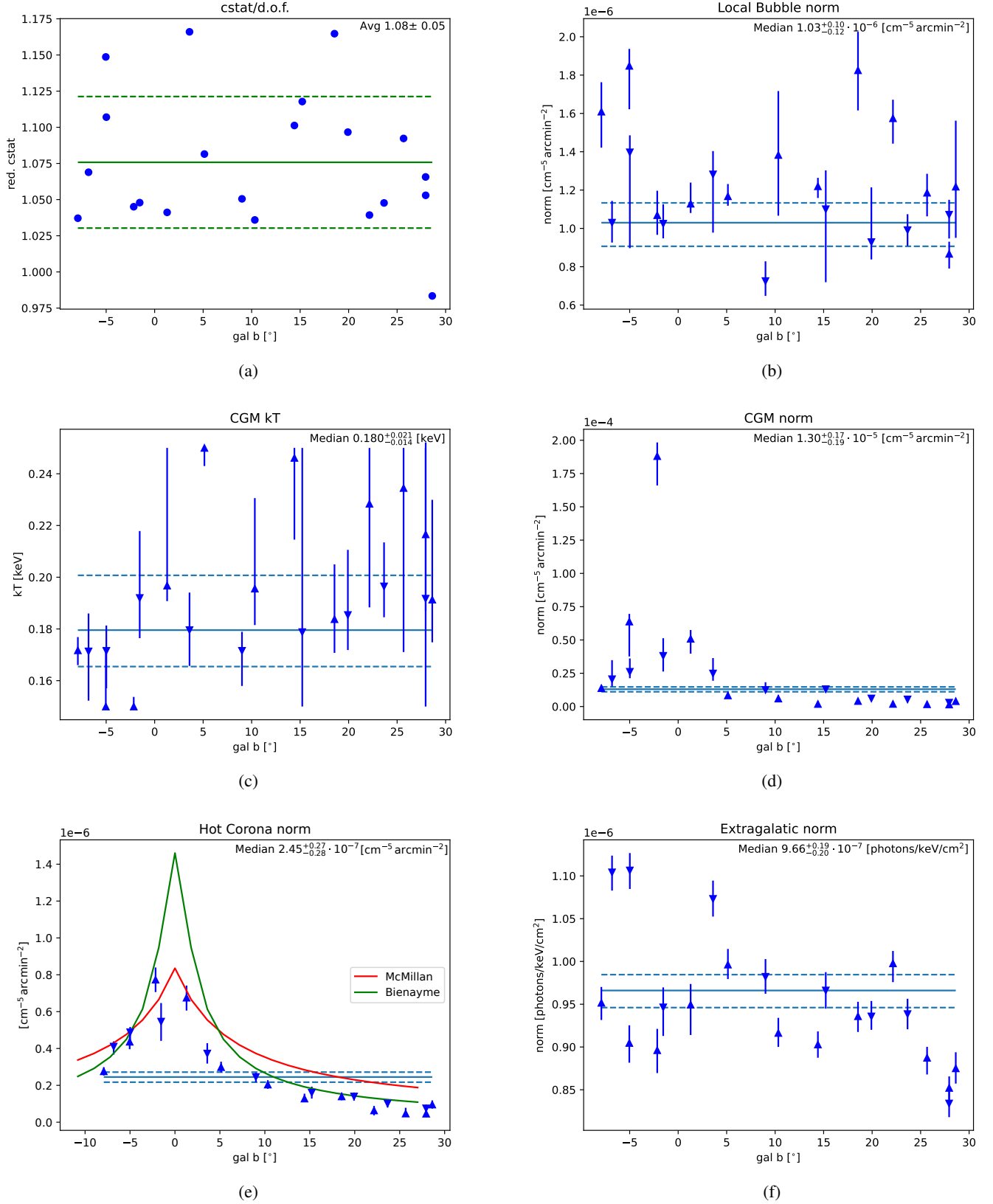


Fig. 9: Variation of the X-ray background model component best-fit parameters over galactic latitude (gal b): (a) Best-fit reduced fit statistic (cstat/d.o.f.). The solid line is the average, while the dashed lines show the 1σ standard deviation. (b) the LHB normalization; (c) the CGM plasma temperature (A_{PEC}); (d) the CGM normalization; (e) the hot corona component normalization ($kT = 0.7$ keV). We also overlaid two Galactic mass profiles, based on Bienayme et al. (1987) and McMillan (2017). The profiles were kindly provided by N. Locatelli, averaged over the projected profiles at $l = 175^\circ - 230^\circ$. The scale of the profiles is arbitrary, chosen for the best visual representation; (f) The extra-galactic component (double-broken-powerlaw) normalization. For (b)-(f) the triangles facing down indicate gal $l < 200^\circ$ while facing up triangles are used for $l > 200^\circ$.

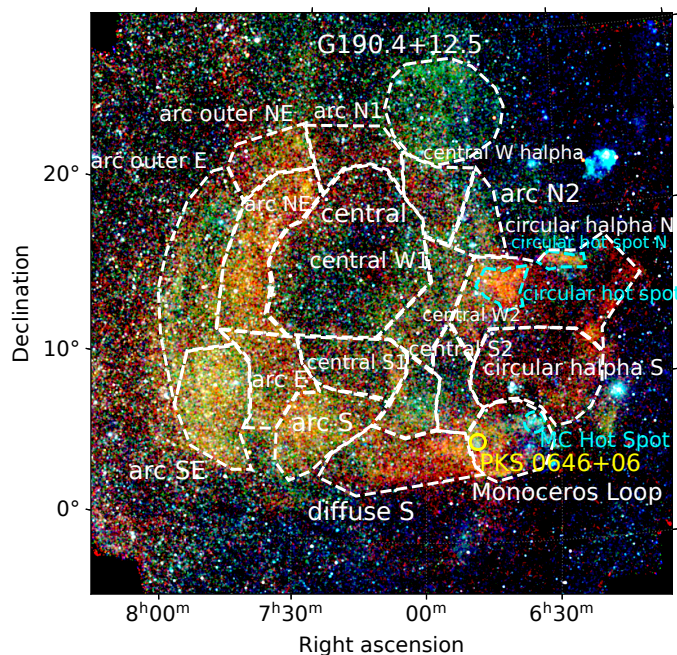


Fig. 10: eROSITA X-ray mosaic as in Fig. 1, with the manually defined regions shown in white and cyan. The cyan regions were defined based primarily on $H\alpha$ emission or are overlapping with another larger region.

method to achieve similar goals. However, the Voronoi binning often leads to bins that include strongly different emission (based on X-ray spectral color) and therefore averaging over different physical conditions is almost unavoidable. The contour-binning method circumvents this problem, with the regions smoothly tracing along any strong gradients in emission.

To obtain regions that are as close as possible to the final statistics of the spectra, we created separate count images based on the same X-ray data. The count images were cleaned of point-sources using similar criteria as for the spectral analysis. In addition, we excluded more complex regions or distinctive objects: G190.4+12.5, Monoceros Loop, and IC443, as well as prominent bright fore- and background sources not associated with the diffuse emission. We did not exposure correct these images, since this would mask any difference in the true statistics. Manually removed solar-flare intervals affected the shape of the regions, since we obtain less counts there. However, the contour-binning method by Sanders (2006) provides parameters to limit the geometry of the bins to some degree. We were able to minimize the effects of the stripe-like low-count regions using the `-CONSTRAINFILL` and `-CONSTRAINVAL=2` parameters. These parameters limits the maximum allowed ratio of the axes of the ellipsoidal extent of the bin, preventing otherwise elongated regions that would follow the shape of the excluded stripes with lower exposure.

We show the resulting contour-bin map in Fig. 11 and the S/N distribution in Fig. 12. In total, we obtained 66 contour-bin regions using this method. All bins fulfill the required minimum S/N of 250. The majority of the bins are centered around the average S/N of 287. We then created masks for each individual contour-bin, including only the respective pixels assigned to the bin. We performed the point-source screening on the mask with the same parameters as before. All pixels that were located inside a $46''$ radius circle of a point-source candidate’s position from the eROSITA catalog was excluded. This allowed us to directly

use the rather complex shapes of the contour bins for extracting the spectra by using `srctool`. For each contour-bin we extracted spectra and calculated response matrices, similar to what we described in Sect. 3. The response matrices were sampled with a size of $2'$, which is accurate enough for the average bin size of the order of a degree or more.

6.2. Model

Similar to the background analysis, we only used the individual spectra of detectors TM1 – 4 and TM6. Again, we used the elemental abundances of `WILM` (Wilms et al. 2000).

For both the contour-bins and manually defined regions, we adopted the background model, with the parameters estimated based on the respective centroid positions, as described in Sect. 5.4. We first introduced an absorbed (`TBABS`) thermal `APEC` component for the source emission, however, the fit quality was bad for some of the regions. Therefore, we instead introduced an absorbed non-equilibrium ionization (NEI) model `NEI` for the source emission for the contour-bins. This significantly improved the fit in the aforementioned regions, indicating that the plasma is in NEI there. For the manually defined regions, due to the higher statistics, we instead used the `VNEI` model that allows to vary individual elemental abundances. In summary, the model described in Eq. 1 was modified to:

$$\begin{aligned} & \text{CONSTANT}_{\text{CAL}} \times \text{CONSTANT}_{\text{A}} \times (\text{ACX2} + \text{APEC}_{\text{LHB}} \\ & \quad + \text{TBABS}_{\text{source}} \times (\text{V})\text{NEI}_{\text{source}} + \\ & \text{TBABS} \times (\text{APEC}_{\text{CGM}} + \text{APEC}_{\text{Corona}} + \text{BKN2POW}_{\text{CXB}})) . \quad (7) \end{aligned}$$

As described above, we constrained the X-ray background parameters to the weighted averages of the four most appropriate background regions, which were determined for each source region/contour-bin individually. The four background regions were chosen based on the lowest Galactic latitude difference to the respective source region. The source component parameters were linked between the different TMs. The detailed spectral fit routine for the contour-bins and manually defined regions is described in Appendix C.

Another issue in the low-count-rate regime is the foreground absorbing column, which is often poorly constrained. Therefore, we utilized the distance integrated A_v dust maps shown in Fig. 5 to estimate the $N_{\text{H,X}}$. We made use of the gas-to-dust ratio derived by Vuong et al. (2003), which is based on *XMM-Newton* data. The gas-to-dust ratio is given as

$$N_{\text{H,X}} = A_j \cdot 7.2(\pm 0.5) \cdot 10^{21} \text{ cm}^{-2} \quad (8)$$

where we used the conversion factor of $A_j = A_v \cdot 0.34^{+0.02}_{-0.04}$ to convert the A_v dust absorption to A_j (Vuong et al. 2003). We mainly applied this estimation to the Monoceros Loop and PKS 0646+06 SNR, but also made consistency-checks with regions of the Monoceros Ring, where we observed indications for absorption. The final results of the spectral analyses are discussed in detail below. In case the source was beyond our map range of > 1.1 kpc, we cross-checked the extinction via the “EXPLORE: G-Tomo” app⁵ which provides profiles up to several kpc. The G-Tomo data is also based on the cube by Lallement et al. (2022), as well as Vergely et al. (2022). However, for most sources the changes in A_v beyond ≈ 1.1 kpc were small and below our sensitivity. The small increase is most likely due to the increasing distance from the Galactic plane and therefore low ISM density.

⁵ <https://explore-platform.eu/sda/g-tomo>

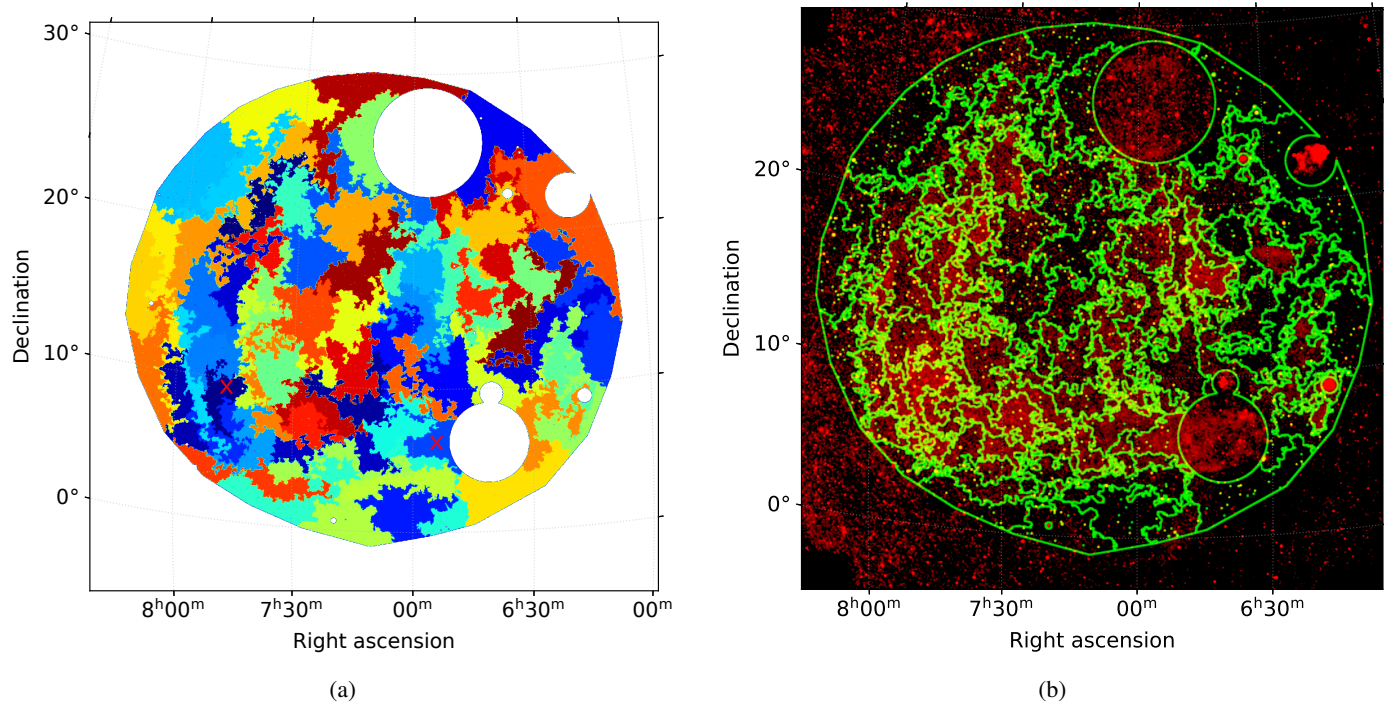


Fig. 11: (a) The map shows the resulting contour-bins with using a minimum S/N of 250. Different colors correspond to different bins. For bins marked with a red “x” we show example spectra in Fig. 13. In (b) an overlay of the bin edges (green) with the eROSITA X-ray image in the 0.20-1.00 keV energy range (red) is shown.

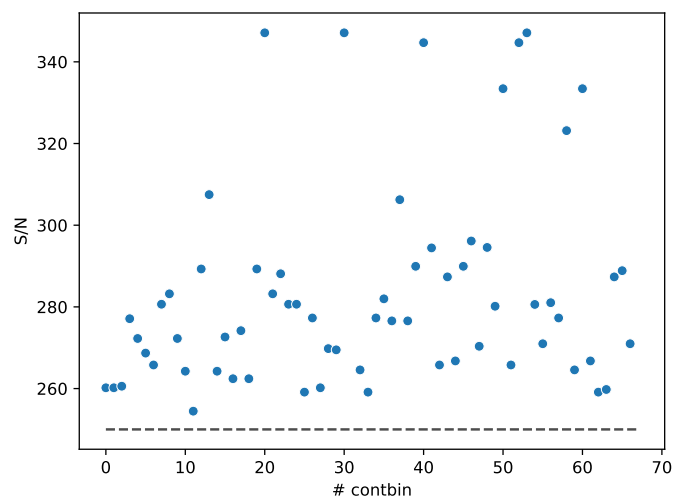


Fig. 12: Distribution of S/N for the contour-bins used for spectra extraction and analysis. The minimum required S/N is shown with a dashed line (250).

6.3. Results

6.3.1. Contour-bins

With our model that uses a simple ν NEI with solar abundances, we achieved very good fits for the entire region, with an average $cstat/d.o.f.$ of 1.08 in a narrow range of 1.00 – 1.22. With our model and unbinned data, $d.o.f. = 1749$ follows for the contour-bins. An example of two contour-bin spectra and best-fit models is shown in Fig. 13. The distribution of $cstat/d.o.f.$ is shown in Fig. 14a.

Thanks to the relatively fine spatial resolution of the contour-bin method, we obtained detailed model parameter maps, as shown in Fig. 14b-Fig. 14d. We derived the median value for the best fit, as well as lower and upper confidence limit values to approximate the overall statistical uncertainty on the median best-fit value. The temperature appears to be relatively uniform, with an average $kT = 0.14 \pm 0.03$ keV for all bins. However, there are several regions that deviate from this mean value. Towards the center of the remnant, coinciding with a lower intensity, we obtain the lowest temperatures $kT \sim 0.09$ keV. In the east (left-handed side) we find a higher plasma temperature, with $kT = 0.18^{+0.02}_{-0.03}$ keV on average, with a significant enhancement towards the south-east with $kT = 0.25^{+0.04}_{-0.05}$ keV (see also Fig. 1, green cross). In addition, we notice an enhancement close to the disk, towards the west. This is most likely caused by the hot plasma of (unresolved) background sources in the Galactic disk.

The ionization timescale (Fig. 14c) shows a gradient approximately from south to north. In the bins where we find an enhanced plasma temperature, we also obtained a relatively low τ , indicating NEI, which extends to the southern part of the remnant. Near the center and west we obtain higher τ , indicating that the plasma might be in CIE here instead. The low τ values in the south and south-east can be interpreted as a lower time since the material was shocked, indicating that those regions are located closer to the shock-front. Alternatively, if we assume that the remnant is very old already, the magnitude of the time since the shock is roughly uniform and low τ values indicate a density gradient. The normalization shown in Fig. 14d corresponds well to the X-ray emission shown in Fig. 1. The bright spot at RA, Dec = $6^{\text{h}}43^{\text{m}}16^{\text{s}}$, $16^{\circ}00'10''$ also appears with the highest normalization of all bins. This region was also observed by Suzaku in our previous study of the Monogem Ring (P2, Knies et al. 2018), where we also obtained the highest normalization with an NEI model.

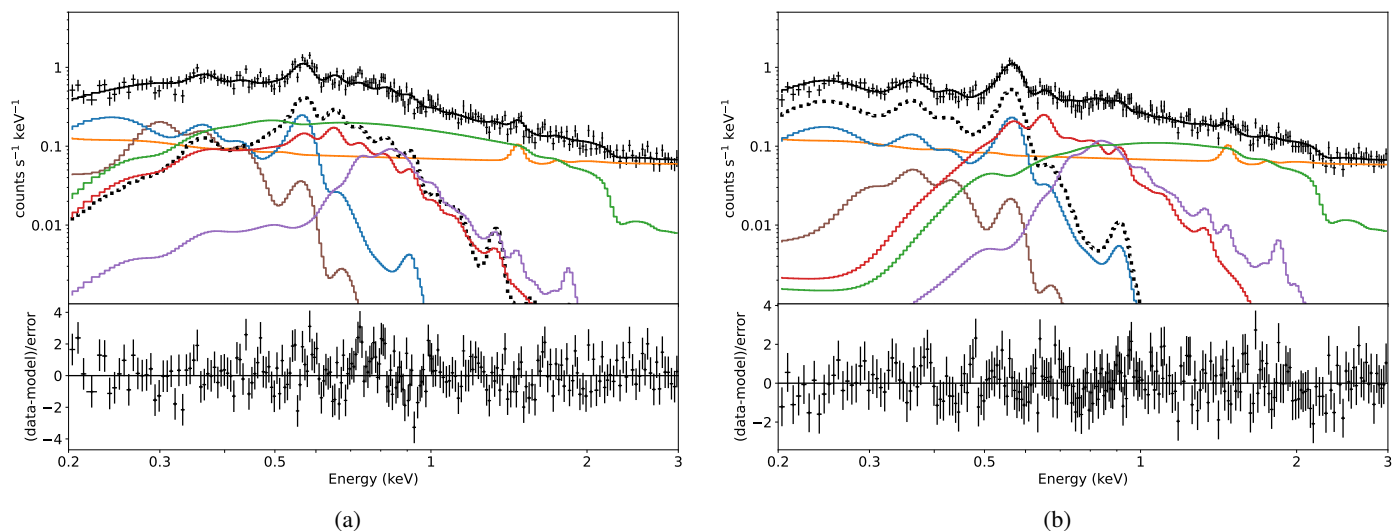


Fig. 13: Two example spectra of contour-bins with the best fit model using the single `NEI` component model for the source. The background is approximated as described above, with the same colors for the various model components as shown in Fig. 8a. The source component is shown with a blue dotted thick line. In (a) we show the spectrum for a bin near the “arc_SE” region and in (b) near the “diffuse_S” region. The corresponding bins are also marked in Fig. 11. For visual purposes only, the spectra were binned with a minimum 5σ or 50 counts per bin and for better visibility only the spectrum and model for TM1 is shown.

6.3.2. Manually defined regions

We first used the model outlined in Eq. 7, that is $\text{TBABS} \times \text{VNEI}$, for the source. The fit results are shown in Table 1. After an initial fit with solar abundances, we used the procedure described in Appendix C to obtain possible non-solar abundances. We show examples of the spectra and best-fit models in Fig. 15 for some of the more interesting regions.

With this model, we obtain very good fits for most regions, with $\text{cstat}/\text{d.o.f.}$ ranging $\sim 0.99 - 1.17$, however, for “arc_SE” we obtain only 1.38. The spectra for this region is shown in Fig. 15a. For the foreground absorption by the TBABS component, we obtain values consistent with zero within uncertainties except for the region “central S1”, however, with small upper limits of only $\sim 10^{20} \text{ cm}^{-2}$. The temperature appears to be consistent with the contour-bin analysis results: low temperatures of $kT \sim 0.08 - 0.15 \text{ keV}$. In the region “arc_SE” we obtain a temperature higher by a factor of about two $kT \sim 0.36 \text{ keV}$. Interestingly, this feature is also obtained with the contour-bin method for bins in the vicinity of this region. The normalization of the diffuse plasma component range $\eta \sim 0.5 - 2.8 \cdot 10^{-6} \text{ cm}^{-5} \text{ arcmin}^{-2}$. The two regions “circular hot spot” (see Fig. 15d) and “circular hot spot N” have one of the highest normalizations among all regions, together with a low temperature $kT \sim 0.11 - 0.12 \text{ keV}$, which explains the bright red morphology observed in Fig. 1.

For only two regions, we obtain non-solar abundances with our initial approach. In the high-temperature region “arc_SE” we obtain a significantly enhanced Si abundance of $5.65^{+1.19}_{-1.00}$ and in the “arc_outer_E” an enhanced O abundance of $3.67^{+0.33}_{-0.73}$, relative to solar. For many of the other regions we also obtain non-solar abundances as best-fit values, however, with high uncertainties that do not rule out solar abundances. Either the plasma is indeed dominated by solar abundances for most parts by the surrounding ISM, or we lack the necessary statistics to measure the non-solar abundances.

We also performed a detailed comparison between the contour-bin method and the manually defined regions, which is discussed in D.

Two-component model: While the non-solar abundance of Si for region “arc_SE” improved the fit significantly, we still obtained poor fit statistics. As we will discuss again below in detail, from the multi-wavelength morphology, we suspect that two different objects might overlap in projection to the south-east. We therefore changed our approach and tried fitting the diffuse emission by using two independent diffuse components, replacing the source components with $\text{TBABS} \times \text{VNEI} + \text{APEC}$, where the absorbed component would represent diffuse plasma located at higher distances, while the unabsorbed APEC would represent the diffuse plasma at low distances. We focused on the regions in the south-eastern part of the (previously assumed) Monogem Ring, where we expect the highest intensity from a possible second component in addition to the Monogem Ring, based on the X-ray morphology. The regions for which we tried the model are listed in Table 2. Additionally, we limited the abundances with possible non-solar values to O, Ne, Si and Fe to reduce the number of free parameters, considering the limited statistics.

The fit results with this approach are shown in Table 2. The spectrum and best-fit model for “arc_SE” is shown in Fig. 15b. With this model, the spectral fits improved significantly for the “arc_SE” and “arc_outer_E” regions, where we also expect the strongest contribution from the possible second, more distant SNR. The temperatures of the hotter component $kT \approx 0.3 - 0.5 \text{ keV}$ are roughly consistent with the previous results, while we obtain significant possible absorption in the upper limits $N_{\text{H}} < 0.4 \cdot 10^{20} \text{ cm}^{-2}$. For the “arc_SE” region, we also obtain enhanced abundances for O and Fe, where the ratio is $\text{Fe}/\text{O} > 1$, typical for Type Ia SN. The higher upper limit absorption in these regions coincide with UV emission observed by Kim et al. (2007, Fig. 1, R1) which could indicate an interaction with denser material here, but due to the large uncertainties this is not conclusive.

In the central regions, the second component temperature is slightly higher compared to the average of the Monogem Ring (using a single component), but still lower compared to the “arc_SE” and “arc_outer_E” regions. If we indeed have two sources overlapping in projection, we measure an average between a hotter distant plasma and the soft emission of the Monogem Ring

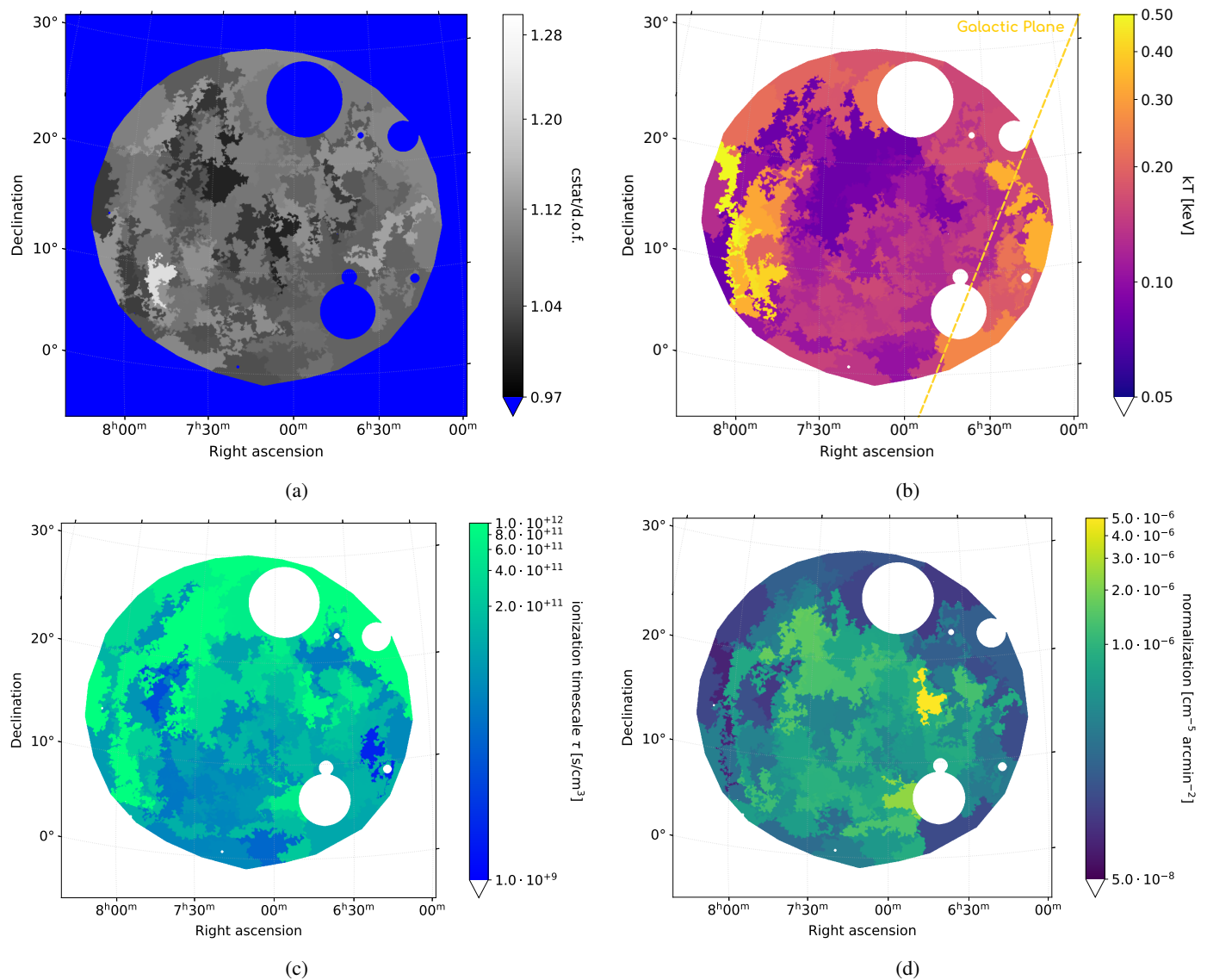


Fig. 14: Spectral analysis results with the contour-binning method, using the `TBABS` \times `NEI` model for the source emission. In (a) we show the red. fit statistic, in (b) the plasma temperature kT , in (c) the ionization timescale τ , and in (d) the normalization of the plasma component, normalized to the respective area of the bins for comparability.

plasma, fitted by a single plasma model component, leads to these results which can be attributed to the limited statistics. For both the "arc_SE" and "arc_outer_E" regions we obtain a relatively high upper limit of the foreground absorption of the hot thermal source component. However, from the A_v maps, we expect very little absorption of $\approx 0.01 \cdot 10^{22} \text{ cm}^{-2}$ at 900 pc for both regions. Therefore, the absorption is not a good indicator of the distance for those regions, far from the Galactic plane.

In order to probe the possible absorption feature we observe in for example Fig. 5b, we also extracted a spectrum from the central part of the X-ray enhancement, matching where the A_v contours are the strongest (i.e. second and third level in Fig. 5b). For this region, we obtain the following expected foreground absorption column, using Eq. 8: $0.007 \cdot 10^{22} \text{ cm}^{-2}$ ($D < 300$ pc), $0.012 \cdot 10^{22} \text{ cm}^{-2}$ ($D < 600$ pc), and $0.126 \cdot 10^{22} \text{ cm}^{-2}$ ($D < 900$ pc). We used a model with two `APEC` components, where the hotter model was multiplied with a `TBABS` absorption component. We obtained a foreground absorption best-fit of $N_H < 0.03 \cdot 10^{22} \text{ cm}^{-2}$ (90% CI). While the upper-limit would be consistent with a distance of

≈ 600 pc, a distance of 900 pc is rejected by our spectral fits. We note, however, that the statistics for this X-ray dark central region are low. Therefore, the result could also indicate a sensitivity limit. Based on the results at hand, the most likely distance to the hotter plasma is $D < 600$ pc, and possibly in line with the distance of the Monogem Ring.

6.3.3. G190.4+12.5

The fit results for G190.4+12.5 are listed in Table 3 and the spectrum and best-fit model is shown in Fig. 16. Here, we again used the simpler `TBABS` \times `VNEI` model to account for the source emission. With our model, we obtain a good fit with cstat/d.o.f. of 1.08. We find a significant foreground absorption to the plasma, with the lower limit of $N_H > 0.17 \cdot 10^{22} \text{ cm}^{-2}$ (90% CI). In comparison, the absorption calculated from the A_v data yields only $N_H \approx 0.12 \cdot 10^{22} \text{ cm}^{-2}$ at the maximum distance of the data at 1.9 kpc (Vergely et al. 2022). The temperature appears to be higher compared to the Monogem Ring, with $kT = 0.42^{+0.43}_{-0.20}$,

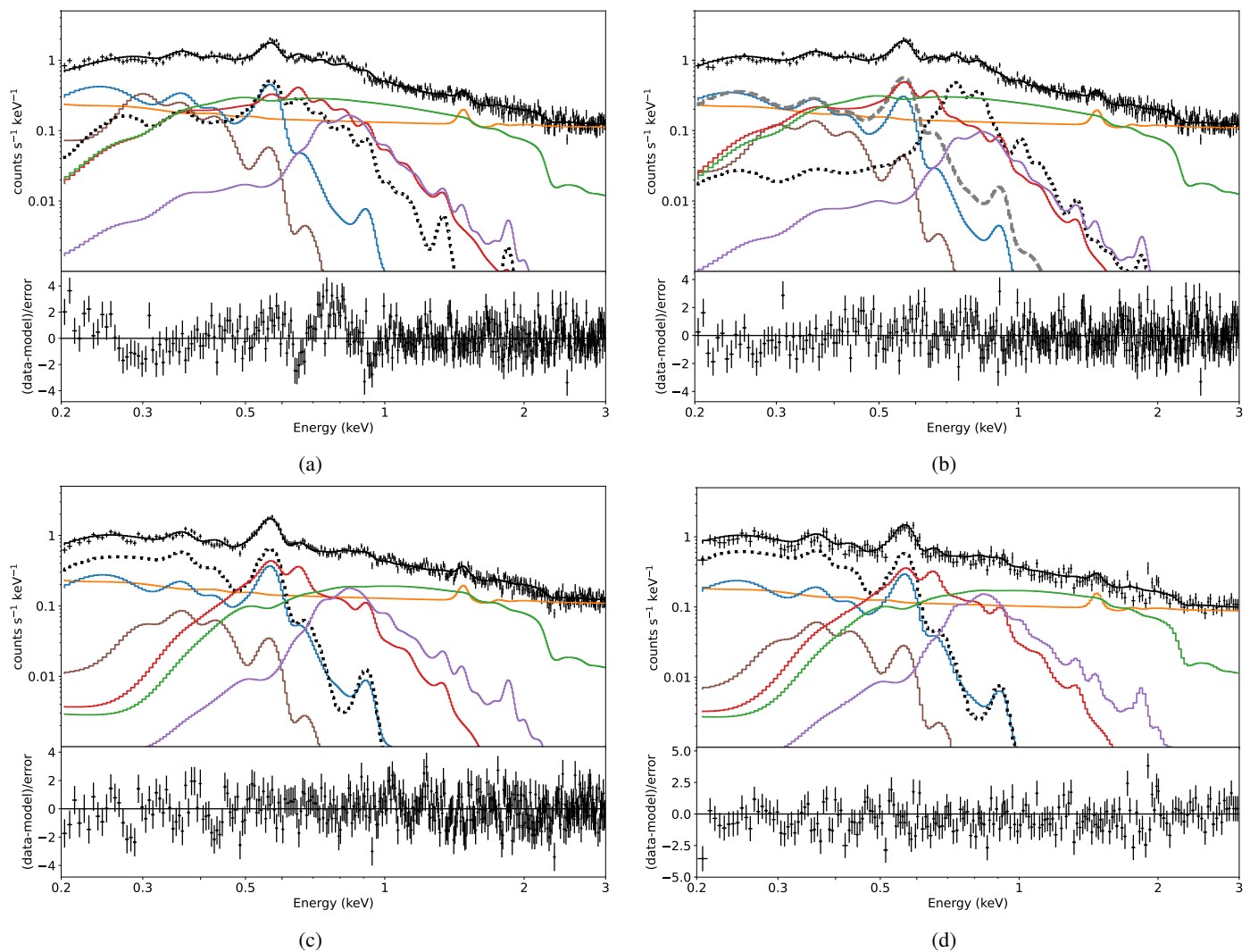


Fig. 15: Spectra and best-fit models for some of the manually defined regions: (a) “arc_SE” with a single vAPEC component and in (b) using vAPEC+APEC for the source. (c) shows the spectrum of the region “diffuse_S” and (d) for the “circular_hot_spot”, both using a single vAPEC component for the source. The visual representation is similar to Fig. 13. In case of the model shown in (b) the second source component (APEC) is shown with a dashed grey thick line.

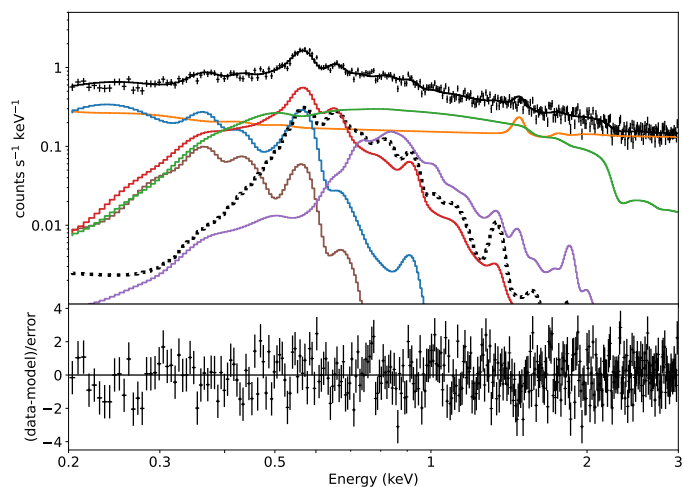


Fig. 16: Spectrum and best-fit model for G190.4+12.5. The source model is $TBABS \times vNEI$. The visual representation is similar to Fig. 13.

however, the uncertainties are large. We also obtain indications for an enhanced O abundance, while the Fe abundance appears to be consistent with solar. The ratio $Fe/O < 1$ appears to be typical for a CC SN, but we lack the statistics to decide which type of SN is favored. The ionization timescale τ is relatively low with $\sim 10^{10} \text{ s cm}^{-3}$, which indicates that either the timescale since the ISM was shocked is short, or the plasma density is low.

6.3.4. Monoceros SNRs

We also analyzed regions of the SNRs Monoceros Loop and PKS 0646+06 using the two-component model already used in the south-eastern part of the Monogem Ring. With only one (absorbed) vNEI model, we were unable to obtain reasonable fits. Introducing an unabsorbed additional APEC significantly improved the fit quality for these regions. From the morphology of the diffuse X-ray emission, it is clear that the soft (red) emission of the Monogem Ring overlaps in projection with the SNRs in the Monoceros vicinity.

The results are shown in Table 4. For all regions, we used the N_H estimate obtained from A_v (see Eq. 8) as lower limit for the

Table 1: Spectral fit results of the manually defined regions. The source model is $\text{TBABS} \times \text{VNEI}$. The abundances were let free to fit and unconstrained or consistent with zero abundances were reset back to solar, as outlined in the text. The uncertainties are equal to the 90% confidence interval (CI).

Region	N_{H} [10^{22} cm^{-2}]	kT [keV]	τ [s/cm^3]	O [solar]	Si [solar]	norm [$\text{cm}^{-5} \text{ arcmin}^{-2}$]	cstat/dof
arc_E	–	$0.126^{+0.011}_{-0.013}$	$(0.47^{+0.37}_{-0.24}) \cdot 10^{11}$	–	–	$(0.79^{+0.17}_{-0.17}) \cdot 10^{-6}$	1.09
arc_N1	–	$0.080^{+0.006}$	$(297.84^{+202.16}_{-289.48}) \cdot 10^{11}$	–	–	$(1.91^{+0.11}_{-0.26}) \cdot 10^{-6}$	1.13
arc_N2	–	$0.081^{+0.013}_{-0.001}$	$(4.90^{+18.70}_{-3.34}) \cdot 10^{11}$	–	–	$(1.43^{+0.34}_{-0.27}) \cdot 10^{-6}$	1.03
arc_NE	–	$0.090^{+0.009}_{-0.090}$	$(3.98^{+496.02}_{-2.19}) \cdot 10^{11}$	–	–	$(1.25^{+0.59}_{-0.32}) \cdot 10^{-6}$	1.09
arc_S	–	$0.149^{+0.010}_{-0.009}$	$(0.43^{+0.23}_{-0.15}) \cdot 10^{11}$	–	–	$(0.73^{+0.11}_{-0.10}) \cdot 10^{-6}$	1.16
arc_SE	–	$0.361^{+0.040}_{-0.041}$	$(0.42^{+0.18}_{-0.10}) \cdot 10^{11}$	–	$5.650^{+1.190}_{-0.998}$	$(0.15^{+0.03}_{-0.02}) \cdot 10^{-6}$	1.38
arc_outer_E	–	$0.080^{+0.011}$	$(7.02^{+493.00}_{-5.03}) \cdot 10^{11}$	$3.670^{+0.330}_{-0.729}$	–	$(0.87^{+0.09}_{-0.33}) \cdot 10^{-6}$	1.08
arc_outer_NE	–	$0.127^{+0.006}_{-0.007}$	$(285.84^{+214.16}_{-272.90}) \cdot 10^{11}$	–	–	$(1.27^{+0.07}_{-0.10}) \cdot 10^{-6}$	1.10
central	–	$0.080^{+0.008}$	$(3.72^{+3.14}_{-1.93}) \cdot 10^{11}$	–	–	$(0.75^{+0.07}_{-0.19}) \cdot 10^{-6}$	1.14
central_S1	$0.003^{+0.007}_{-0.003}$	$0.136^{+0.015}_{-0.014}$	$(0.59^{+0.28}_{-0.17}) \cdot 10^{11}$	–	–	$(0.59^{+0.07}_{-0.11}) \cdot 10^{-6}$	1.13
central_S2	–	$0.144^{+0.005}_{-0.013}$	$(2.79^{+0.92}_{-0.69}) \cdot 10^{11}$	–	–	$(1.04^{+0.12}_{-0.08}) \cdot 10^{-6}$	1.07
central_W1	–	$0.122^{+0.008}_{-0.012}$	$(1.36^{+1.42}_{-0.59}) \cdot 10^{11}$	–	–	$(0.84^{+0.16}_{-0.15}) \cdot 10^{-6}$	1.10
central_W2	–	$0.153^{+0.014}_{-0.010}$	$(0.31^{+0.22}_{-0.13}) \cdot 10^{11}$	–	–	$(0.50^{+0.11}_{-0.09}) \cdot 10^{-6}$	1.06
central_W_half	–	$0.140^{+0.031}_{-0.014}$	$(0.63^{+0.86}_{-0.36}) \cdot 10^{11}$	–	–	$(0.53^{+0.10}_{-0.05}) \cdot 10^{-6}$	0.99
circular_half_N	–	$0.120^{+0.007}_{-0.004}$	$(1.61^{+1.24}_{-0.40}) \cdot 10^{11}$	–	–	$(1.04^{+0.13}_{-0.10}) \cdot 10^{-6}$	1.14
circular_half_S	–	$0.136^{+0.005}_{-0.017}$	$(1.57^{+0.84}_{-0.55}) \cdot 10^{11}$	–	–	$(0.83^{+0.09}_{-0.11}) \cdot 10^{-6}$	1.17
circular_hot_spot	–	$0.109^{+0.003}_{-0.010}$	$(1.65^{+1.27}_{-0.41}) \cdot 10^{11}$	–	–	$(2.75^{+0.65}_{-0.24}) \cdot 10^{-6}$	1.10
circular_hot_spot_N	–	$0.110^{+0.011}_{-0.017}$	$(1.09^{+1.88}_{-0.63}) \cdot 10^{11}$	–	–	$(1.54^{+0.83}_{-0.39}) \cdot 10^{-6}$	1.11
diffuse_S	–	$0.122^{+0.006}_{-0.008}$	$(1.02^{+0.34}_{-0.25}) \cdot 10^{11}$	–	–	$(1.39^{+0.40}_{-0.05}) \cdot 10^{-6}$	1.14

Table 2: Results from selected regions in the south-east, fitted with a two-plasma spectral model. The source model is $\text{TBABS} \times \text{VAPEC}_1 + \text{APEC}_2$, where the absorbed VAPEC component represents the hotter diffuse emission in the back, and the APEC the unabsorbed soft emission in the front.

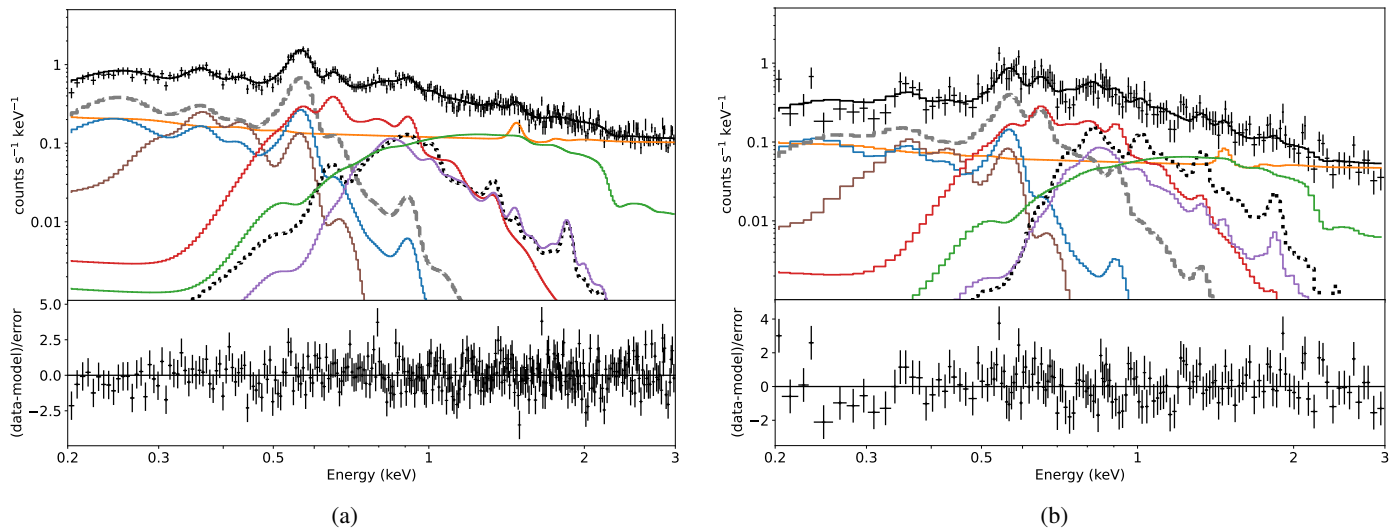
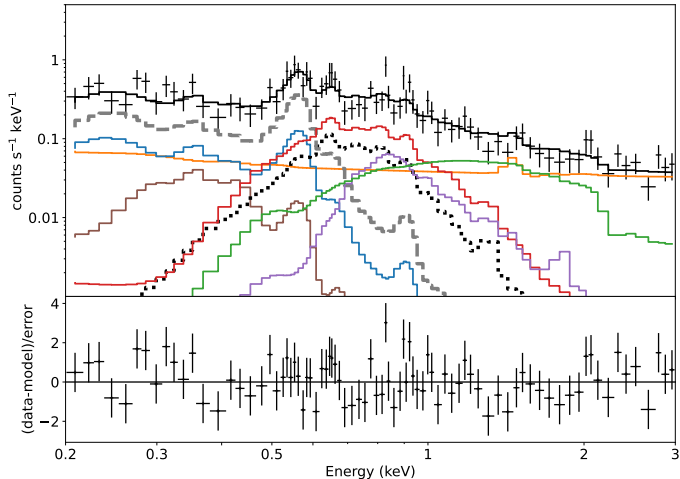
Region	N_{H} [10^{22} cm^{-2}]	kT_1 [keV]	O_1 [solar]	Fe_1 [solar]	norm ₁ [$\text{cm}^{-5} \text{ arcmin}^{-2}$]	kT_2 [keV]	norm ₂ [$\text{cm}^{-5} \text{ arcmin}^{-2}$]	cstat/dof
arc_E	$0.000^{+0.314}$	$0.130^{+0.021}_{-0.130}$	$2.100^{+7.900}_{-2.050}$	$0.098^{+9.900}_{-0.048}$	$(0.53^{+0.32}_{-0.51}) \cdot 10^{-6}$	$0.089^{+0.029}_{-0.018}$	$(1.18^{+0.45}_{-0.66}) \cdot 10^{-6}$	1.08
arc_S	$0.009^{+0.008}_{-0.003}$	$0.130^{+0.009}_{-0.130}$	$1.320^{+0.251}_{-0.028}$	$0.098^{+2.390}_{-0.098}$	$(1.46^{+0.16}_{-0.62}) \cdot 10^{-6}$	$0.086^{+0.037}_{-0.018}$	$(0.49^{+0.50}_{-0.44}) \cdot 10^{-6}$	1.16
arc_SE	$0.000^{+0.412}$	$0.426^{+0.021}_{-0.043}$	$2.080^{+3.270}_{-1.030}$	$3.490^{+4.680}_{-1.320}$	$(0.14^{+0.07}_{-0.08}) \cdot 10^{-6}$	$0.125^{+0.004}_{-0.004}$	$(1.27^{+0.07}_{-0.09}) \cdot 10^{-6}$	1.07
arc_outer_E	$0.000^{+0.231}$	$0.339^{+0.058}_{-0.061}$	$1.190^{+0.440}_{-0.384}$	$1.340^{+0.530}_{-0.375}$	$(0.37^{+0.16}_{-0.11}) \cdot 10^{-6}$	$0.115^{+0.005}_{-0.006}$	$(0.70^{+0.06}_{-0.08}) \cdot 10^{-6}$	1.05
central	$0.000^{+0.005}$	$0.187^{+0.004}_{-0.006}$	$1.320^{+0.324}_{-0.205}$	$0.098^{+0.239}_{-0.098}$	$(0.30^{+0.06}_{-0.09}) \cdot 10^{-6}$	$0.082^{+0.011}_{-0.007}$	$(1.06^{+0.24}_{-0.22}) \cdot 10^{-6}$	1.09
central_S2	$0.013^{+0.055}_{-0.013}$	$0.197^{+0.058}_{-0.050}$	$0.098^{+1.290}_{-0.098}$	$2.920^{+3.900}_{-1.850}$	$(0.20^{+1.04}_{-0.10}) \cdot 10^{-6}$	$0.152^{+0.003}_{-0.120}$	$(0.79^{+0.03}_{-0.39}) \cdot 10^{-6}$	1.06
central_W1	$0.000^{+0.020}$	$0.164^{+0.016}_{-0.021}$	$1.140^{+0.581}_{-0.320}$	$0.098^{+0.679}_{-0.098}$	$(0.37^{+0.47}_{-0.18}) \cdot 10^{-6}$	$0.107^{+0.013}_{-0.030}$	$(0.84^{+0.26}_{-0.54}) \cdot 10^{-6}$	1.09

foreground absorption of the VNEI component. We obtain good fits with cstat/d.o.f. 1.03 – 1.11 using this model. The temperature of the unabsorbed APEC appears to be consistent between the Monoceros Loop and PKS 0646+06 and the mean temperature for the Monogem Ring. These results indicate, that we indeed fit the soft emission with the second, unabsorbed plasma component. For the Monoceros Loop "Hot Spot" the temperature appears to be enhanced in comparison. This is most likely caused by the hotter emission of the Monoceros Loop, overlapping in addition to the soft emission of the Monogem Ring. The normalization also appears to be similar and typical to the values derived from the contour bins, where some local variation beyond the statistical error is expected.

The Monoceros Loop appears to have a high temperature of $kT = 0.968^{+0.165}_{-0.102}$ keV with a low $\tau = (0.94^{+0.41}_{-0.29}) \cdot 10^{11} \text{ s cm}^{-3}$. The foreground absorbing column is fitted with the lower limit, but appears to be constrained towards higher values. A previous study found a much lower temperature of only ~ 0.2 keV (Leahy et al. 1985). Most likely, the authors - due to a lack of spatial and spectral resolution - were fitting primarily the foreground emission of the Monogem Ring overlapping with the emission from Monoceros Loop, which lead to a much lower temperature, effectively averaging all plasma components in the line of sight. Interestingly, the "Hot Spot" of the Monoceros Loop, visible as a bright knot in the X-ray images, appears to have a lower temperature. At the same time, the normalization appears to be

Table 3: Spectral fit results for G190.4+12.5, using the source model $\text{TBABS} \times \text{VNEI}$. For the norm, we were unable to determine reliable uncertainties.

N_{H}	kT	O	Fe	τ	norm	cstat/dof
$[10^{22} \text{ cm}^{-2}]$	[keV]	[solar]	[solar]	$[\text{s}/\text{cm}^3]$	$[\text{cm}^{-5} \text{ arcmin}^{-2}]$	
$0.29^{+0.32}_{-0.12}$	$0.42^{+0.43}_{-0.20}$	$1.84^{+0.43}_{-0.42}$	$0.73^{+0.32}_{-0.21}$	$(2.53^{+11.4}_{-1.75}) \cdot 10^{10}$	$1.91 \cdot 10^{-7}$	1.09


 Fig. 17: Spectra and best-fit models for (a) the Monoceros Loop SNR and (b) the ‘‘Hot Spot’’ region inside the Monoceros Loop, rebinned visually with 3σ or 30 counts. The source model is $\text{TBABS} \times \text{VNEI} + \text{APEC}$ for both. The visual representation is similar to Fig. 13. The second source component (APEC) is shown with a dashed grey thick line.

 Fig. 18: Spectrum and best-fit model for PKS 0646+06, rebinned visually with 3σ or 30 counts. The source model is $\text{TBABS} \times \text{VNEI} + \text{APEC}$. The visual representation is similar to Fig. 13. The second source component (APEC) is shown with a dashed grey thick line.

higher by a factor ~ 20 and the τ indicates that the plasma is in CIE, or has a high density. Possibly, this emission originates from a previously cold, dense cloud that was shocked by the SNR blast wave. We show the spectra and best-fit models for both regions in Fig. 17.

For the more distant PKS 0646+06 we also obtained a good fit with the two-component model, with cstat/d.o.f. of 1.06. The temperature also appears to be relatively high with $kT \sim 0.6 - 1.0$ keV, while the ionization timescale is low with $\tau < 10^{11} \text{ s cm}^{-3}$. Here, we had to freeze the foreground absorption to the value derived from A_v due to low statistics, resulting in the parameter not being well constrained otherwise. A previous study by Leahy (1986) found a much lower temperature of $kT \sim 0.1 - 0.2$ keV which again leads us to believe that they instead were mainly sensitive to the foreground emission of the Monogem Ring. The spectrum and best-fit model is shown in Fig. 18.

7. Properties of the SNRs

7.1. Determining the center

Monogem Ring: Determining the SN’s point of origin is central to estimate characteristic properties such as the age and explosion energy. In our previous study, based on ROSAT and Suzaku observations, we determined a center close to PSR B0656+14 (Thorsett et al. 2003; Knies et al. 2018). With the new data, we obtained a much clearer picture of the diffuse emission in the vicinity of the Gemini-Monoceros X-ray enhancement. Instead of a manual approach based on the morphology, we decided to use the BANANA tool, originally developed for bubble detection, based on Minkowski tensors (Collischon et al. 2021). This tool provides a relatively unbiased way to determine the center of the diffuse structure, based on the emission. As we have discussed in Sect. 4, the different energy bands show different features, and therefore morphology. We determined the center in two different bands: 0.2-0.4 and 0.4-0.8 keV.

Table 4: Spectral fit results for the Monoceros SNRs. The source model is $\text{TBABS} \times \text{VNEI}_1 + \text{APEC}_2$, where the absorbed VAPEC component represents the hotter diffuse emission in the back, and the APEC the unabsorbed Monogem Ring emission.

Region	N_{H} [10^{22} cm^{-2}]	kT_1 [keV]	τ [s/cm^3]	norm_1 [$\text{cm}^{-5} \text{ arcmin}^{-2}$]	kT_2 [keV]	norm_2 [$\text{cm}^{-5} \text{ arcmin}^{-2}$]	cstat/dof
MC ¹	$0.282^{+0.067}$	$0.968^{+0.165}_{-0.102}$	$(0.94^{+0.41}_{-0.29}) \cdot 10^{11}$	$(0.23^{+0.04}_{-0.04}) \cdot 10^{-6}$	$0.133^{+0.005}_{-0.004}$	$(1.50^{+0.07}_{-0.11}) \cdot 10^{-6}$	1.11
MC HS ²	$1.040^{+0.156}_{-0.208}$	$0.467^{+0.138}_{-0.107}$	$> 1.00 \cdot 10^{11}$	$(5.83^{+4.62}_{-2.43}) \cdot 10^{-6}$	$0.194^{+0.012}_{-0.014}$	$(1.27^{+0.10}_{-0.10}) \cdot 10^{-6}$	1.07
PKS ³	0.245	$0.773^{+0.279}_{-0.134}$	$(0.66^{+0.40}_{-0.40}) \cdot 10^{11}$	$(0.74^{+0.17}_{-0.21}) \cdot 10^{-6}$	$0.147^{+0.016}_{-0.015}$	$(2.35^{+0.34}_{-0.24}) \cdot 10^{-6}$	1.06

¹ Monoceros Loop; ² Monoceros Loop Hot Spot; ³ PKS 0646+06

Since BANANA - simply speaking - calculates lines perpendicular to edges, we first processed the images using a Gaussian gradient magnitude (GGM) filtering (Sanders et al. 2016). This highlights the features we are most interested in: the shell-like filaments in the diffuse emission. We applied the GGM filter with a filter size of 4 pixels to binned images (factor 2) in the respective bands, where we removed the bottom 0.1% and top 1% percentiles of the brightness distribution to reduce outliers. Additionally, we excluded point-source candidates with the list already used for the spectral analysis. Holes were filled with surrounding pixel values using the `astropy.convolve` function.

The GGM convolved maps were then used as input for BANANA. We chose the length of the calculated lines sufficiently long to allow possible intersections over the entire structure. The thresholds for the calculations were based on the 80-99.9% percentile range of the GGM maps to focus on the strongest features. The line-density maps were smoothed in a final step with a diameter of 200 pixels. This was necessary, since the X-ray morphology is clearly not a well-defined shell as typically seen in young supernova remnants. This leads to the lines not intersecting exactly in the same spot, since they are perpendicular to the edges that are significantly distorted from a perfect circle. Instead, we have an "area" of intersection. Using the smoothing, we can reconstruct the position where the line-density is the highest. The results are shown in Fig. 19a for 0.2-0.4 keV (soft) and Fig. 19b for 0.4-0.8 keV (medium). We find a clear difference in the recovered center position, depending on the analyzed energy band. For the soft band the position with the highest line density is close to the position of the pulsar candidate, albeit with a relatively low accuracy (Fig. 19a). For the medium band, we find two clear maxima, one close to $7^{\text{h}}30^{\text{m}}$, 15° and the other one to the west, with some smaller enhancements to the northwest.

From this analysis, we recover two possible center positions for the Monogem Ring SNR. One is based on the soft emission and appears to be close to the previously assumed center (Knies et al. 2018) and associated pulsar position. The second possible center position was calculated from the medium band and appears to be significantly different from the pulsar position. It is unclear if the diffuse emission originates from the same structure, since the shape of the diffuse emission changes significantly between the different bands. The recovered line-density maxima suggest that we are instead dealing with two distinct overlapping structures: the Monogem Ring SNR being the larger structure, with a center near $6^{\text{h}}58^{\text{m}}$, $14^{\circ}44'$, and another slightly smaller ring-like structure with the center near $7^{\text{h}}23^{\text{m}}$, $12^{\circ}16'$ (Green Arc and edge of green emission Fig. 2). Another explanation would be a highly asymmetric and distorted morphology due to a strong surrounding ISM density gradient, as well as the likely high age.

Monoceros Loop, PKS 0646+06 and G190.4+12.5: For PKS 0646+06 (G206.9+2.3) we used the center position from the SNR catalog by Green (2019) at RA, Dec = $6^{\text{h}}48^{\text{m}}40^{\text{s}}$, $6^{\circ}26'$, and a radius of $25' \pm 2.5'$, resulting in a size of $50' \times 50'$. Since the morphology of the Monoceros Loop and G190.4+12.5 candidate are well defined shell-like, we directly determined the size and center positions from the X-ray images by hand. We defined circular regions so that the shell-like filaments of the respective object overlapped with the circle. For the Monoceros Loop we obtained the center position at RA, Dec = $6^{\text{h}}40^{\text{m}}57^{\text{s}}$, $6^{\circ}11'05''$ with a radius of $2.13^{\circ} \pm 0.21^{\circ}$, based on the morphology. This position deviates from the one reported by Green (2019) by $\sim 0.5^{\circ}$ with a radius larger by $\sim 9\%$, however, the previously reported position and extent does not align well with the X-ray morphology. Similarly, for G190.4+12.5, we obtain the center at RA, Dec = $6^{\text{h}}57^{\text{m}}48^{\text{s}}$, $25^{\circ}30'14''$ with a radius of $3.28^{\circ} \pm 0.33^{\circ}$. We assume an uncertainty of 10% on the radius for each SNR.

7.2. Constraining the distance

Without a secure compact object counter-part of an SNR, distance estimates are challenging. One way to indirectly determine the distance of an SNR is by determining the foreground absorption. The absorption by dust is a good tracer for colder material, which absorbs X-rays on the way from the source to us. The 3D dust absorption map by Lallement et al. (2022) is perfectly suited for constraining the distance to any object that shows anti-correlation in the emission.

To make use of the 3D information in the map by Lallement et al. (2022), we integrated the dust absorption A_{v} along the line of sight in distance slices: 0-300 pc, 300-600 pc, 600-900 pc, and 900-1120 pc. Since soft X-rays are more sensitive to absorption (Wilms et al. 2000), we overlaid contours of the dust slices with the soft X-ray maps, as shown in Fig. 5a-Fig. 5c. We do not show the map up to 300 pc since it is relatively feature-less in the vicinity of the Monogem Ring (i.e. no significant absorption). We note, however, that the dust contours trace the outer Edges of the X-ray emission to some degree (i.e. anti-correlation).

In the slice 300-600pc (Fig. 5a) we already see features that overlap with the X-ray emission. Towards the south the soft X-ray emission shows no anti-correlation with the dust contours. This indicates that this part of the diffuse extended X-ray emission must be located at ~ 300 pc or closer. At 600-900 pc we note several interesting features. There appears to be an absorption feature located near the center of the diffuse X-ray emission. This region also shows a low surface brightness in X-rays. Interestingly, the dust contours directly south of the center show no correlation whatsoever with the X-ray emission. However, the N_{H} we ob-

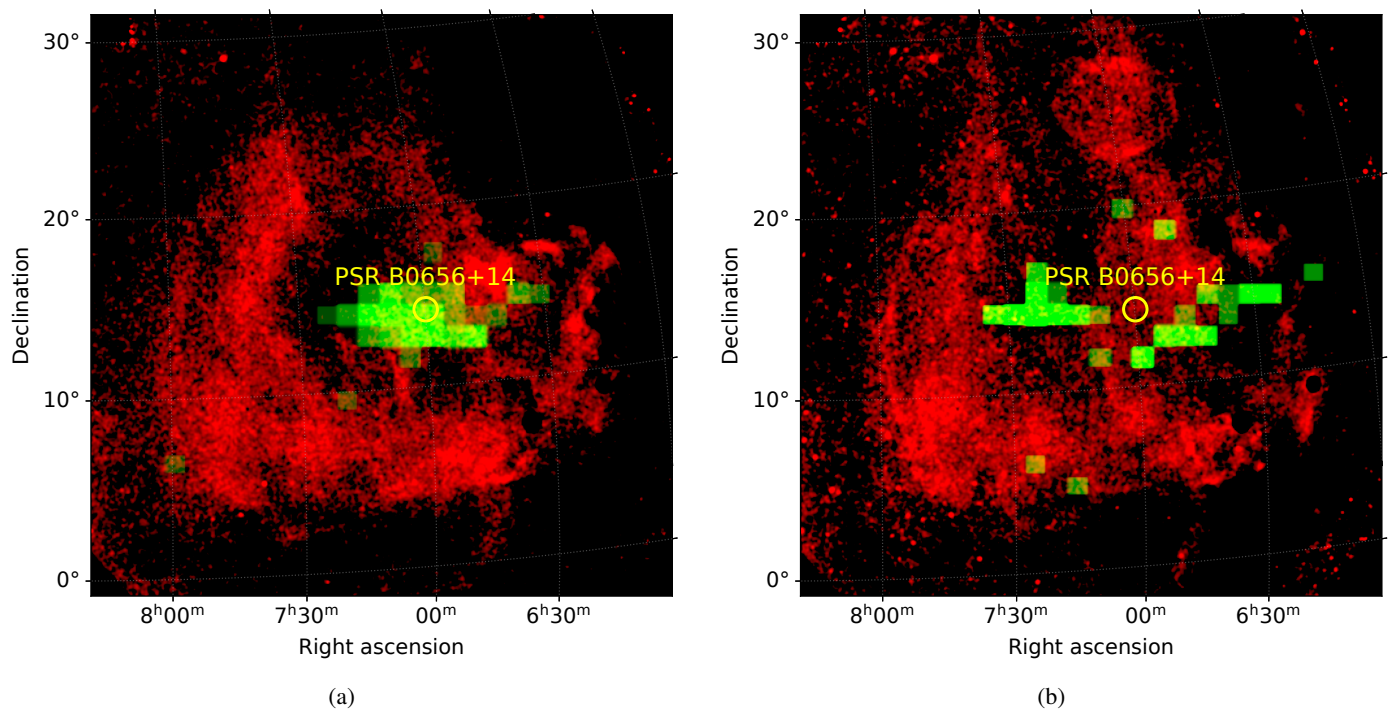


Fig. 19: The eROSITA X-ray images (red), overlaid with the line-density maps derived from the GGM convolved X-ray images, using BANANA (green). Higher line-densities correspond to brighter colors. In (a) we show in the X-ray image and line density in 0.2 – 0.4 keV and (b) for 0.4 – 0.8 keV. Also shown is the position of the compact object PSR B0656+14 in yellow.

tained from the spectral analysis of the region overlapping with the A_p feature limits the distance to < 600 pc. There are several possible implications from this:

- If we assume, as in previous studies, that the whole diffuse structure (sans Monoceros Loop and PKS 0646+06) is only one object and located at a distance of ~ 300 pc, the apparent anti-correlation in the center is purely coincidental and the absorbing feature instead located behind the diffuse plasma. In this case, the lower background emission due to the absorption feature, together with a lower surface brightness in the center of the remnant might mimic an anti-correlation. The low upper limits of the absorption column from the spectral fits supports the chance coincidence. This would also explain why we see no anti-correlation in other parts of the remnant.
- If we instead assume the superposition of two objects at different distances, the absorption feature would put the Monogem Ring SNR at the previously determined $D = 300$ pc, since the absorption features for $D > 300$ pc overlap with the soft diffuse emission without any anti-correlation. Furthermore, another ring-like diffuse structure would be located at larger distances > 600 pc which is visible with green emission in Fig. 1. This ring-like structure then would explain the perfect anti-correlation in the center of the remnant between X-rays and the A_p data for the distance slice of 600–900 pc. However, our spectral analysis puts an upper limit of $D < 600$ pc on the plasma distance, whether or not it belongs to the Monogem Ring or another, second SNR. This leaves the possibility of a second SNR at roughly the same distance than the Monogem Ring. As we will discuss below, this scenario best fits our findings.

At higher distances > 900 pc we see no anti-correlation between the contours and X-rays from the Monogem Ring SNR anymore. Therefore it is safe to assume that most of the diffuse emission

must be located < 900 pc (except the Monoceros SNRs and the new SNR candidate).

7.3. Discussion

From the spectral analysis and multi-wavelength data, it is difficult to decide whether the larger structure known as the Monogem Ring SNR could instead be composed of two individual SNRs. The completely different plasma properties near the “Green Arc” (Fig. 2) make it difficult to just explain the difference by an asymmetry in the expansion or initial explosion alone (T , norm, τ , abundance). In addition, if we assume two distinct SNRs, this shifts the approximate geometric center of the Monogem Ring to the north-west in the frame of Fig. 2 which could solve the long-standing discrepancy of the proper motion of PSR B0656+14, currently moving towards the geometric center of the SNR (Thorsett et al. 2003). With the geometry as shown in Fig. 20 we obtain a geometric center located very close to the birthplace of the pulsar, and indeed the current proper motion of the pulsar points away from the center, as expected. Moreover, the center of the new candidate G205.6+12.4 is only 1.5° away from the center recovered from the medium band with BANANA, as shown in Fig. 19b. A small difference is expected since the true dynamic center is difficult to determine precisely for very old remnants. Therefore, assuming two remnants at roughly the same distance ($D = 300 - 500$ pc) elegantly explains all our findings without the need to rely on extreme asymmetries in the SNR evolution or SN explosion. In the following we will consider that the previously believed monolithic structure “Monogem Ring” consists of two individual old SNRs, however, we stress that assuming only one remnant at $D = 300$ pc, our results are still in line with previous findings, as we discuss later.

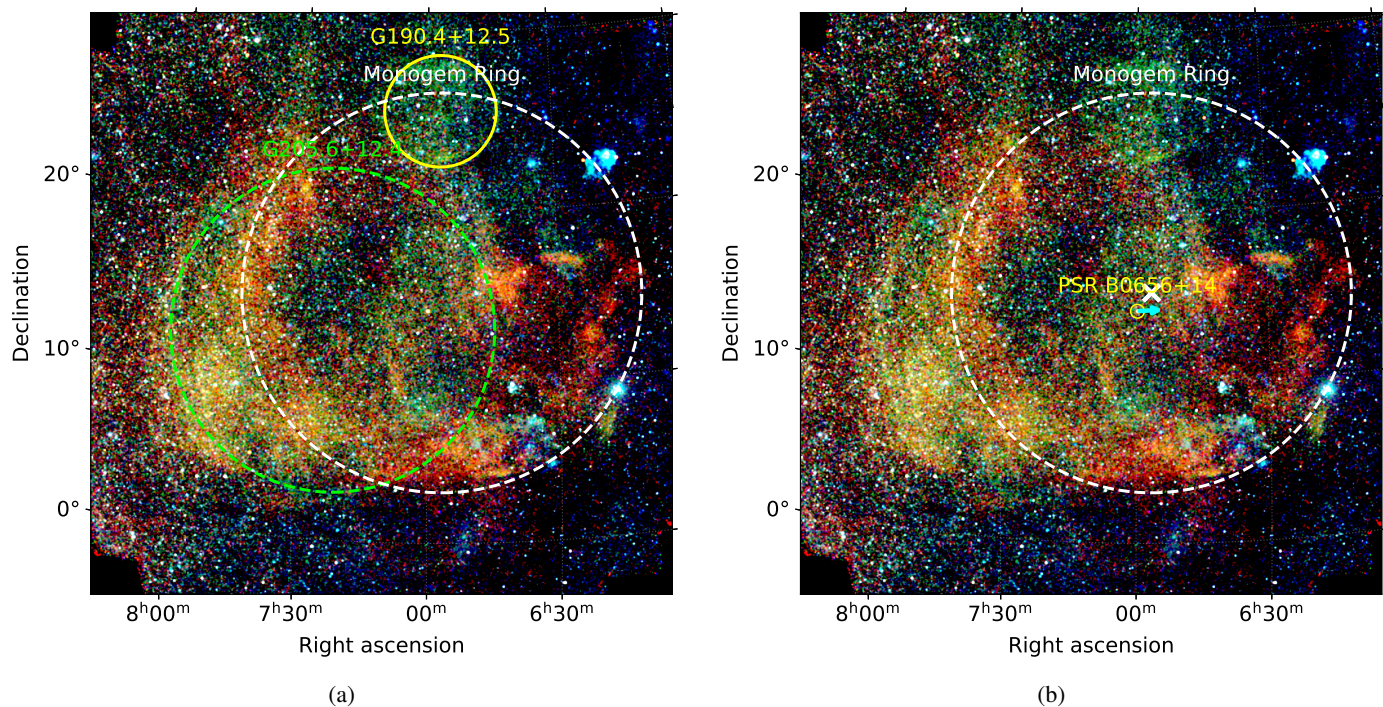


Fig. 20: (a) eROSITA X-ray mosaic as in Fig. 1, with the estimated geometry of the SNRs based on the X-ray morphology. The Monogem Ring is shown with dashed white, G205.6+12.4 in dashed green, and G190.4+12.5 in yellow. (b) eROSITA X-ray mosaic as in Fig. 1, with the geometric center of the Monogem Ring as a white X, the current position of PSR B0656+14 as yellow circle, and the origin of the pulsar with a cyan arrow (Briskin et al. 2003). The arrow takes into account the proper motion of the pulsar (Briskin et al. 2003) with the end of the arrow pointing at the birthplace.

7.4. 3D model

For a better visualization of the geometry of the three SNRs in the proximity of the Monogem Ring, we created a 3D view shown in Fig. 21. We assumed the distances as indicated in the figure, and projected the Galactic (l, b) accordingly to obtain absolute x , y , and z coordinates in units pc.

7.5. Estimations

We used the results from the spectral analyses to estimate the characteristics of the SNRs and SNR candidates. For this, we used a modified version of SNRpy by Leahy et al. (2017). Originally, this tool provides a graphical interface to calculate SNR properties based on a set of input parameters and SNR evolution models (e.g., Sedov-Taylor). We modified the code to provide a grid of SNR evolutionary models for a range of input parameters, such as different ambient densities, ages, and explosion energies. We calculated grids with 15,000 distinct SNR models by varying the input parameters for two evolutionary models: Sedov-Taylor (e.g., Taylor 1950; Truelove & McKee 1999) and the cloudy ISM model (White & Long 1991). Despite the name, all evolutionary phases of an SNR are calculated for both models (not limited only to the Sedov phase).

The parameter ranges for the grid were determined as follows. The explosion energy E_0 of the supernova is widely unknown without additional information, therefore, we constrained the parameter range to a reasonable range of $E_0 = (0.1 - 2.0) \cdot 10^{51}$ erg, based on simulations (Müller et al. 2016). From the spectral analysis we can derive the pre-shock density, as shown below. We used our lowest derived value as a lower limit of n_0 , and literature values as upper limits. We take the value of $n_0 \approx 0.06 \text{ cm}^{-3}$

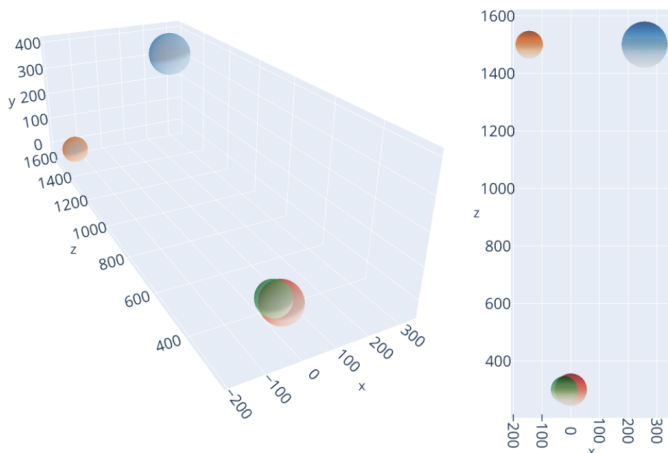


Fig. 21: 3D geometrical model of the Gemini-Monoceros X-ray enhancement based on our results: perspective (left) and orthographic top view (right). The units of the coordinates are pc, with the axes being: Galactic longitude distance relative to the Monogem Ring x , with the Monogem Ring at $x = 0$, distance from the Galactic plane y , and the distance z from us. The different colored spheres indicate the different SNR (candidates) with the correct radius at the respective assumed distance. The Monogem Ring is shown in red and G205.6+12.4 in green at $D = 300$ pc, the Monoceros Loop SNR at $D = 1500$ pc in orange, and G190.4+12.5 in blue at $D = 1500$ pc (assumed distances).

from the study by Elwood et al. (2017) as the upper limit, which appears to be consistent with other measurements, as the authors show. For the values derived from our spectral analysis we took

the respective uncertainties into account. In summary, the grids cover the ranges of $n_0 = 0.5 \cdot 10^{-3} - 0.06 \text{ cm}^{-3}$ for the ambient density, $E_0 = (0.1 - 2.0) \cdot 10^{51} \text{ erg}$ for the explosion energy, and $t_0 = 5000 - 140,000 \text{ yr}$ for the age.

In the next step, to constrain the possible SNR evolutionary parameter space, we used the X-ray temperature derived from the kT values of the spectral analysis results. We compared this with the predicted X-ray temperature of the respective model. We take the emission measure (EM) weighted temperature, which should be close to the measured X-ray temperature of the plasma (Leahy et al. 2017). The models and regions from which we take the input parameters are also referenced in Table 5. For the Monogem Ring SNR, we also estimated the plasma properties from the annulus shown in Fig. A.1, that is only taking the brighter shell parts into account, to derive median values from the spectral fit parameters. The parameters were estimated from the contour-bin regions Fig. 14.

From the spectral analysis, we can derive the ISM density with the normalization η of the APEC or NEI model via the EM, given as:

$$\text{EM} = \eta \cdot \left(\frac{10^{-14}}{4\pi D^2} \right)^{-1} = \int n_e n_H dV. \quad (9)$$

As shown by Hamilton et al. (1983), for SNRs in the Sedov phase with a radial density profile the EM is related to the electron and hydrogen densities by

$$\text{EM} = 2.07 \left(\frac{n_e}{n_H} \right) n_{H,0}^2 V f, \quad (10)$$

where V is the SNR's volume, f the filling factor and n_e , n_H the electron and hydrogen densities of the plasma, respectively. From this, the pre-shock density n_0 , that is the ambient ISM density, can be estimated by assuming $n_e/n_H = 1.21$ and $n_0 \approx 1.1 n_{H,0}$ (Kavanagh et al. 2022). To estimate the volume V , we assumed a sphere with the center positions and radii shown in Table 5 for the respective SNR. The pre-shock density n_0 was used to further narrow down the range of possible SNR evolutionary parameters. Finally, an additional constraint was put by comparing the predicted SNR radius with the radius estimated from the geometry of the respective remnant, assuming an uncertainty of 10%.

Monogem Ring: The SNR evolutionary models for the Monogem Ring are shown in Fig. 22 assuming a distance of $D = 300 \text{ pc}$ and geometry as shown in Fig. 20, by assuming two remnants. The SNR models agree with our analysis results for relatively high ages $\approx 110,000 \text{ yr}$, higher by about $\sim 30\%$ to previous age estimates of $\sim 70,000 - 86,000 \text{ yr}$ (Plucinsky et al. 1996; Knies et al. 2018). Our estimated ambient density agree with both the pure Sedov-Taylor model and the cloudy ISM model. Both models suggest a low explosion energy, with the Sedov-Taylor estimation lower by at least a factor of two with $E_0 \sim (0.1 - 0.2) \cdot 10^{51} \text{ erg}$. With the cloudy ISM model we obtain $E_0 \sim (0.2 - 0.4) \cdot 10^{51} \text{ erg}$ which appears more realistic, suggesting that colder, dense ISM was situated in the vicinity prior to the explosion.

The multi-wavelength observations in the vicinity show that the Monogem Ring could be surrounded by denser ISM in several directions. Towards the Galactic disk we observe significant $H\alpha$ emission that appears to be anti-correlated with the Monogem Ring. Additionally, Kim et al. (2007) observed UV emission here, which they interpreted as possible interactions between the SNR's shock and colder, dense ISM. Towards the south (Fig. 1 frame), close to the region "diffuse_S", they also observed strong UV

emission. This indicates, that the remnant could indeed be partially surrounded by dense ISM, favoring the cloudy ISM model. With this model, the mean age consistent with the density estimates is $\sim 1.1 - 1.2 \cdot 10^5 \text{ yr}$ which agrees surprisingly well with the age determined for the pulsar PSR B0656+14 to $\sim 1.1 \cdot 10^5 \text{ yr}$ (Thorsett et al. 2003; Zharikov et al. 2021).

If we instead assume a single SNR as shown in Fig. A.1 and use the parameters for a single SNR described in Table 5, we obtain an age higher by only $\sim 5\%$ with similar explosion energies. The combination of a larger radius, lower density and larger temperature range balance each other. In that scenario, the asymmetric morphology and high-temperature region in the south-east might be explained by a blow-out after encountering a denser region (Reynolds 2017). Another possibility would be a highly asymmetric initial explosion together with a very strong surrounding ISM density gradient prior to the explosion.

SNR candidate G205.6+12.4: If we assume the geometry as shown in Fig. 20, we obtain the parameters for the SNR model calculations as shown in Table 5. Due to the slightly larger distance from the Galactic plane, we expect less dense or clumpy ISM. Therefore we show only the Sedov-Taylor estimation in this discussion. The estimated ambient ISM density is also consistent with a higher distance from the Galactic plane. We note, that we also obtain valid solutions with the clumpy ISM model (with a slightly lower predicted age). The possible SNR parameters are shown in Fig. 23 for an assumed distance of $D = 300 \text{ pc}$. Within our estimated ambient density range, we obtain ages from $40,000 - 55,000 \text{ yr}$. The possible explosion energies appear to be similar to the Monogem Ring, with $E_0 \sim (0.2 - 0.3) \cdot 10^{51} \text{ erg}$.

We also calculated models for $D = 200$, however, here we don't find any SNR model that matches with our properties derived from the spectral analysis. For higher distances we do get SNR models up to 500 pc that match our results, with the main difference being a slightly higher age and explosion energy with increasing distance. Therefore, we can constrain the distance to the SNR candidate to $\approx 300 - 500 \text{ pc}$.

SNR candidate G190.4+12.5: For this object, we obtain low ambient densities, as shown in the SNR model parameter diagram in Fig. 24. For the estimated possible ISM densities, we find SNR configurations in the full range of $E_0 = (0.1 - 2.0) \cdot 10^{51} \text{ erg}$, with ages in the range $40,000 \text{ yr}$ to $100,000 \text{ yr}$. If this object is indeed an SNR, it would be situated well above the Galactic plane, which explains the low ISM densities we obtained. The almost perfectly circular morphology also suggests that the expansion of the remnant appeared to be freely and relatively uniform. A younger age of $40,000 - 60,000 \text{ yr}$ is favored, while the higher ages are found only for a very narrow parameter range at very low explosion energies. Due to the large uncertainties on the X-ray spectral fit parameters, we are only able to give a lower limit on the distance of $> 1.5 \text{ kpc}$ for this SNR candidate. While the N_H lower limits discussed in Sect. 6.3.3 hint towards a distance of $> 2 \text{ kpc}$, the A_v data is very limited at large distances, especially further away from the Galactic plane. Above $2 - 3 \text{ kpc}$, the geometric radius becomes too large while also requiring unrealistically small ISM densities.

Monoceros Loop: The possible models for the Monoceros Loop SNR are shown in Fig. 25 for the distance $D \approx 1.5 \text{ kpc}$. We adopted this distance from the study by Leahy et al. (1986). Other studies suggest a distance of $\sim 1.6 \text{ kpc}$ (Graham et al. 1982; Xiao

Table 5: Parameters used for the estimation of the SNRs' properties. For the radius, we assume an uncertainty of 10%, while the temperature and density uncertainties are based on the 90% CI of the spectral analysis results. For the density, f denotes the filling factor of the plasma.

Remnant/Distance	Center (RA, Dec)	Radius	Region	Model	kT [keV]	$n_0 f^{-1/2}$ [10^{-3} cm $^{-3}$]	R [pc]
Single SNR at $D = 300$ pc							
Monogem Ring $D = 300$ pc	107.08°, 13.50°	11.97°	annulus (median)	Fig. 14 Fig. A.1	0.11 – 0.17	3.1 – 7.2	63
Two SNRs at $D = 300$ pc							
Monogem Ring G205.6+12.4	104.15°, 15.30°	11.00°	diffuse_S	Table 1	0.11 – 0.13	5.5 – 8.6	58
	110.33°, 12.94°	8.82°	arc_outer_E + arc_SE	Table 2	0.28 – 0.45		47
G190.4+12.5 $D = 1000$ pc $D = 1500$ pc $D = 2000$ pc	104.24°, 25.56°	3.07°	-	Table 3	0.22 – 0.85	1.9 – 3.3 1.5 – 2.7 1.3 – 2.3	53 80 107
Monoceros Loop SNRs							
Monoceros Loop $D = 1500$ pc	100.24°, 6.18°	2.13°	-	Table 4 [†]	0.87 – 1.13	2.1 – 3.4	56
PKS 0646+06 $D = 4000$ pc	102.16°, 6.42°	0.42°	-	Table 4 [†]	0.64 – 1.05	4.9 – 8.7	29

[†] hot vAPEC plasma component used

& Zhu 2012), however, within uncertainties this does not change the interpretation of our results. While the density appears to be low, the radio study by Xiao & Zhu (2012) suggests, that the SN explosion might have taken place in a low-density cavity, created by several massive stars. Our results suggest a low age of only up to $\sim 40,000$ yr. Lower ages of $\sim 30,000$ yr are favored, with explosion energies of at least $> 0.8 \cdot 10^{51}$ erg. This is in good agreement with previous studies, that obtained an age of $\sim 30,000$ yr as well (Leahy et al. 1985; Welsh et al. 2001). We were able to disentangle the plasma emission in the line of sight into distinct components, thus getting a more accurate estimation on the properties of the X-ray emitting plasma and reducing the contamination of the soft foreground emission of the Monogem Ring. The resulting higher X-ray temperature suggests a rather high explosion energy.

PKS 0646+06: For this remnant, we assumed a distance of 4 kpc for the SNR estimations. Previous studies suggest a range from 3 – 5 kpc (Graham et al. 1982; Gao et al. 2011). We find relatively low explosion energies of $(0.2 - 0.4) \cdot 10^{51}$ erg. The remnant appears to be in the Sedov phase with ages ranging 15,000 – 20,000 yr. The previous X-ray study by Leahy (1986) found a much higher age of $\sim 60,000$ yr, most likely caused by modeling primarily the contaminating foreground emission of the Monogem Ring with $kT \approx 0.14$ keV in their analysis. A study based on optical line emission by Ambrocio-Cruz et al. (2014) estimate a lower distance of ~ 2.2 kpc and an age of $6.4 \cdot 10^4$ yr. However, they require a very low explosion energy of $1.7 \cdot 10^{49}$ erg and derive a much lower shock velocity compared to our results from X-rays. Instead, this indicates that the remnant might interact with dense cold clouds in the vicinity. Both the

low explosion energy together with a high age are rejected by our analysis.

8. Summary

In this work, we performed a morphological and spectral analysis of the entire Gemini-Monoceros X-ray enhancement for the first time, using novel eROSITA data of the first four all-sky surveys. We performed a careful background analysis across the entire field to create a predictive background model for all source regions. The source regions were defined both statistically, as well as manually, and we extract and modeled spectra for each of the regions, obtaining detailed plasma model parameter maps with fine spatial resolution. Our most important results are as follows:

- Most of the diffuse emission attributed to the Monogem Ring can be described well with an unabsorbed thermal plasma in NEI with a low average temperature of $kT \sim 0.14 \pm 0.03$ keV. However, in the regions in the south-east (Green Arc, Fig. 2) of the Monogem Ring, a second, hotter plasma component is necessary to achieve good spectral fits. This component has a temperature of $kT > 0.28$ keV, in addition to the low-temperature component of the Monogem Ring. The morphology indicates the presence of an arc-like temperature enhancement with harder (green) X-ray color, which is reproduced by the high temperature component when extending the two-plasma model to the entire field. Although statistics are limited, the abundances for the south-eastern hot plasma are typical for a type Ia supernova, while the colder plasma component is consistent with solar abundances. A dust absorption features at 600 – 900 pc appears to be anti-correlated with the X-ray emission in the center. However, we found no

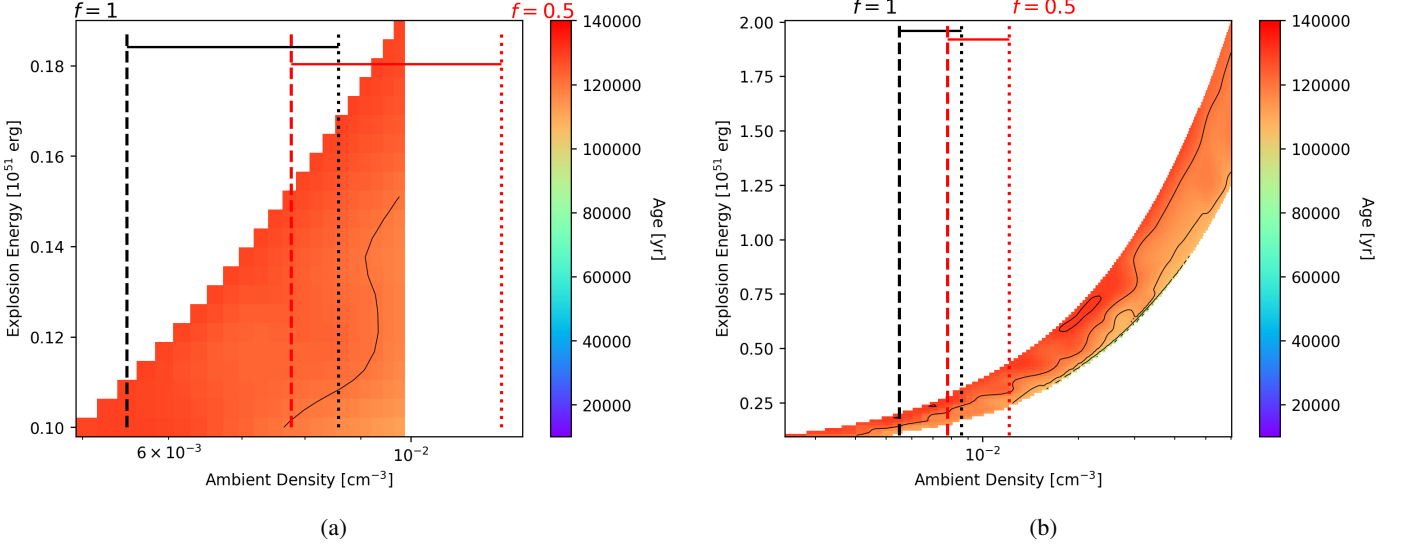


Fig. 22: SNR model parameters for the Monogem Ring SNR, assuming a radius of 58.3 pc at $D = 300$ pc. The estimated uncertainty on the radius is 10%. The color scale indicates the calculated age of the respective model. The vertical dashed and dotted lines show the ambient ISM density n_0 lower and upper limits, respectively, for different filling factors. The density n_0 was inferred from the spectral analysis for $D = 300$ pc. The black dashed and dotted lines show n_0 for $f = 1$, while the red lines show n_0 for $f = 0.5$. Models with predicted radii and X-ray temperatures outside the derived confidence intervals are not shown. The SNR evolutionary models are Sedov-Taylor (a) and Cloudy ISM (b) for $\tau = 2$ (Leahy et al. 2017). The color scale for the age is in absolute values for better comparability with the other SNRs. The black solid contours on top of the surface plot denote different levels of the age in steps of 10,000 yr, similar to the color scale shown on the right.

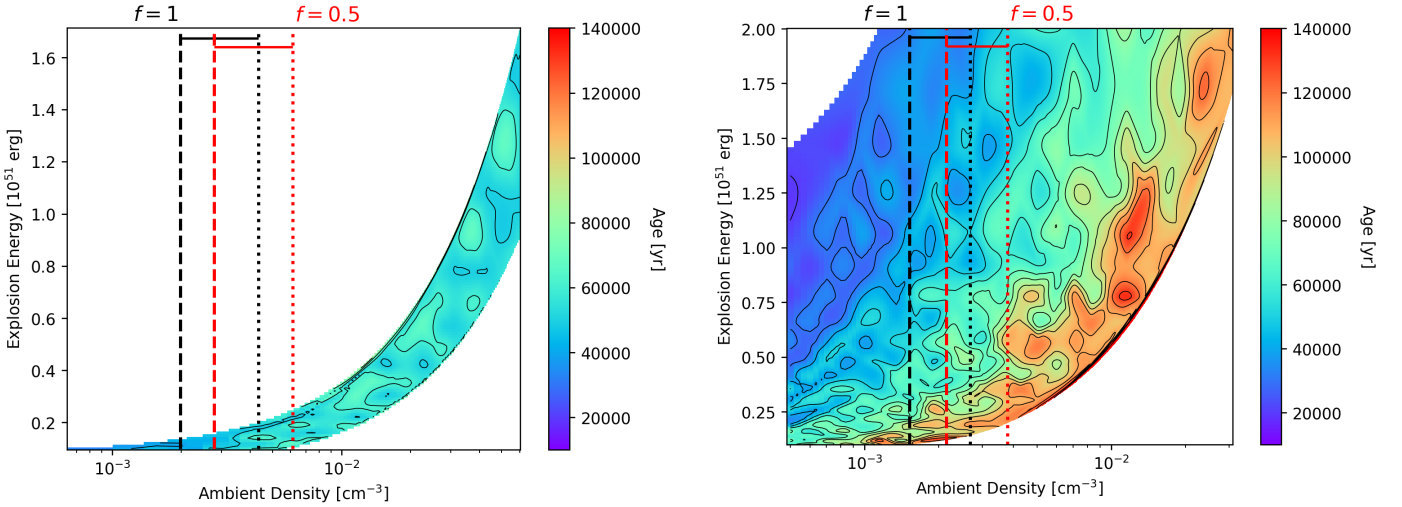


Fig. 23: As in Fig. 22, but for the G205.6+12.4, using the Sedov-Taylor model. The assumed distance is $D = 300$ pc, which yields a radius of 47 pc.

Fig. 24: As in Fig. 22, but for G190.4+12.5, using the Sedov-Taylor model. The assumed distance is $D = 1500$ pc, which yields a radius of 80.4 pc.

significant N_{H} in the spectral fits, putting an upper limit of $D < 600$ pc on the plasma.

- We showed, that a second remnant at roughly the same distance as the Monogem Ring SNR ($D = 300 - 500$ pc) explains our results well. In this configuration, the center of the Monogem Ring would be shifted in a direction, which would lead to a more favorable agreement between the proper motion of PSR B0656+14 and the Monogem Ring SNR. A second remnant would also explain the different plasma conditions near the “Green Arc” in the south-east. This candidate would have an age of 40,000 – 85,000 yr and explosion energy of

$0.2 - 0.6 \cdot 10^{51}$ erg, depending on the distance. No compact object was found near the approximate center in the given distance range.

- For the Monogem Ring, if we assume a single SNR, we obtain an age similar to the age of PSR B0656+14 and explosion energies typical for a CC SN, albeit on the lower end. We obtain similar results when assuming two SNRs, with slightly lower explosion energies and 5% lower age, even more consistent with the age of the pulsar.
- We found a new SNR candidate at $(l, b) \sim (190.4^\circ, 12.5^\circ)$ with a radius of $\sim 3^\circ$, that shows up as an almost perfect

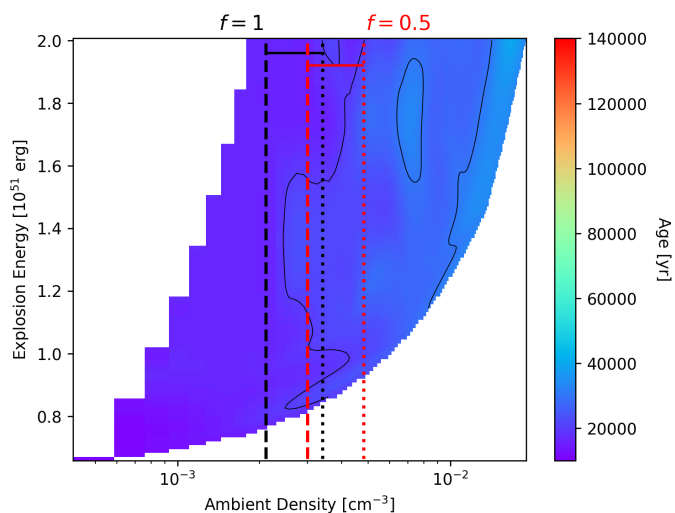


Fig. 25: As in Fig. 22, but for the Monoceros Loop SNR candidate, using the Sedov-Taylor model. The assumed distance is $D = 1500$ pc, which yields a radius of 55.8 pc.

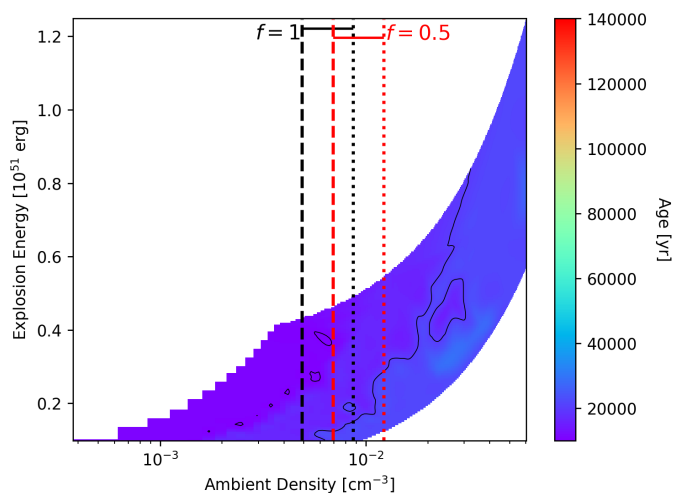


Fig. 26: As in Fig. 22, but for PKS 0646+06, using the Sedov-Taylor model. The assumed distance is $D = 4000$ pc, which yields a radius of 29.1 pc.

circular diffuse structure for X-ray images with $E > 0.4$ keV. We obtained significant foreground absorption to the plasma, and a temperature of ~ 0.4 keV, with the plasma being in NEI. For a distance of ~ 1.5 kpc we estimate an age of $\sim 40,000 - 60,000$ yr. Due to relatively high uncertainties of the spectral fit results, we are able to constrain the explosion energy only to a lower limit of $> 0.2 \cdot 10^{51}$ erg.

- We analyzed the Monoceros Loop and PKS 0646+06 SNRs and improved on previous studies with the new data. We were able to disentangle the X-ray emission in the line-of-sight into the low-temperature foreground emission by the Monogem Ring and higher-temperature emission by the SNRs. Previous studies did not take into account the contamination by the foreground emission, therefore, we obtained significantly higher temperatures for the SNRs’ plasma. For the Monoceros Loop, we estimate a “young” age of $\sim 20,000$ yr and relatively high explosion energies of $> 0.7 \cdot 10^{51}$ erg. The expansion appears to take place into a low-density environment,

consistent with previous studies. For the more distant PKS 0646+06 we find an age of only 15,000 – 20,000 yr, much lower compared to previous studies, and the remnant appears to be in the Sedov phase.

Our results strengthen the association of the Monogem Ring SNR with PSR B0656+14 and provide the most detailed spectral analysis of the diffuse emission so far. We studied the highly asymmetric morphology of the SNR and found a high temperature enhancement to the south-east. We found indications of a possible second SNR at a similar distance than the Monogem Ring SNR, both from the spectral analysis and multi-wavelength data. This SNR candidate, dubbed G205.6+12.4, appears to have a similar explosion energy and an age of 40,000 – 55,000 yr, about half the age compared to the Monogem Ring if located at $D = 300$ pc. A distance beyond $D > 600$ pc is rejected by our analysis. However, statistics are low to definitively claim two SNRs instead of only the “Monogem Ring”. Further, deep observations are required to confirm or reject the newly discovered SNR candidate.

Moreover, we analyzed the Monoceros Loop SNR and PKS 0646+06 for the first time with CCD resolution spectra and an accurate background model, which revealed different properties than derived in previous studies. We also found a new SNR candidate (G190.4+12.5) at high Galactic latitudes and distances > 1.5 kpc located at the edge of the Monogem Ring. Low limit our prediction accuracy for this candidate, however, the energetics are consistent with a SN explosion. The remnant appears to expand into a very low density ambient medium with an age of $\sim 40,000 - 60,000$ yr. Further dedicated pointed observations of this object might help to confirm this object as an SNR and determine its properties with higher precision.

The newly discovered faint old SNRs could explain part of the “missing SNR” problem in our Galaxy. As concluded by Ranasinghe & Leahy (2022), even for low distances $D < 1$ kpc around the Sun, about half of the expected SNRs are missing. Since those objects are too faint in radio, full-sky X-ray surveys similar as performed by eROSITA might be able to explain the discrepancy for the nearby SNR density in the future.

Acknowledgments

We thank N. Locatelli and M. Sormani for providing the re-projected mass profiles of the Milky Way. We also thank Jeremy Sanders for helpful advice in applying the contour-binning method. This work is based on data from eROSITA, the soft X-ray instrument aboard SRG, a joint Russian-German science mission supported by the Russian Space Agency (Roskosmos), in the interests of the Russian Academy of Sciences represented by its Space Research Institute (IKI), and the Deutsches Zentrum für Luft- und Raumfahrt (DLR). The SRG spacecraft was built by Lavochkin Association (NPOL) and its subcontractors, and is operated by NPOL with support from the Max Planck Institute for Extraterrestrial Physics (MPE). The development and construction of the eROSITA X-ray instrument was led by MPE, with contributions from the Dr. Karl Remeis Observatory Bamberg & ECAP (FAU Erlangen-Nuernberg), the University of Hamburg Observatory, the Leibniz Institute for Astrophysics Potsdam (AIP), and the Institute for Astronomy and Astrophysics of the University of Tübingen, with the support of DLR and the Max Planck Society. The Argelander Institute for Astronomy of the University of Bonn and the Ludwig Maximilians Universität Munich also participated in the science preparation for eROSITA. The eROSITA data shown here were processed using the eSASS/NRTA software system developed by the German eROSITA consortium. Parts

of the acknowledgements were compiled using the Astronomy Acknowledgement Generator. This research has made use of data and/or software provided by the High Energy Astrophysics Science Archive Research Center (HEASARC), which is a service of the Astrophysics Science Division at NASA/GSFC and the High Energy Astrophysics Division of the Smithsonian Astrophysical Observatory. This research has made use of the VizieR catalogue access tool, CDS, Strasbourg, France. This research made use of Astropy, a community-developed core Python package for Astronomy (Astropy Collaboration et al. 2018, 2013) This research made use of matplotlib, a Python library for publication quality graphics (Hunter 2007) This research made use of NumPy (Harris et al. 2020) This research made use of XSPEC (Arnaud 1996) This research made use of ds9, a tool for data visualization supported by the Chandra X-ray Science Center (CXC) and the High Energy Astrophysics Science Archive Center (HEASARC) with support from the JWST Mission office at the Space Telescope Science Institute for 3D visualization. Some of the results in this paper have been derived using the healpy and HEALPix packages.

This work was supported by the Deutsche Forschungsgemeinschaft through the project SA 2131/13-1. M.S. acknowledges support from the Deutsche Forschungsgemeinschaft through the grants SA 2131/14-1 and SA 2131/15-1. GP acknowledges financial support from the European Research Council (ERC) under the European Union’s Horizon 2020 research and innovation program “HotMilk” (grant agreement No. 865637) and support from Bando per il Finanziamento della Ricerca Fondamentale 2022 dell’Istituto Nazionale di Astrofisica (INAF): GO Large program and from the Framework per l’Attrazione e il Rafforzamento delle Eccellenze (FARE) per la ricerca in Italia (R20L5S39T9).

References

- Ambrocio-Cruz, P., Rosado, M., Le Coarer, E., Bernal, A., & Gutiérrez, L. 2014, *Rev. Mexicana Astron. Astrofis.*, 50, 323
- Anderson, L. D., Wang, Y., Bühr, S., et al. 2017, *A&A*, 605, A58
- Arnaud, K. A. 1996, in *Astronomical Society of the Pacific Conference Series*, Vol. 101, *Astronomical Data Analysis Software and Systems V*, ed. G. H. Jacoby & J. Barnes, 17
- Astropy Collaboration, Price-Whelan, A. M., Sipőcz, B. M., et al. 2018, *AJ*, 156, 123
- Astropy Collaboration, Robitaille, T. P., Tollerud, E. J., et al. 2013, *A&A*, 558, A33
- Bienayme, O., Robin, A. C., & Creze, M. 1987, *A&A*, 180, 94
- Bregman, J. N., Anderson, M. E., Miller, M. J., et al. 2018, *ApJ*, 862, 3
- Brisken, W. F., Thorsett, S. E., Golden, A., & Goss, W. M. 2003, *ApJ*, 593, L89
- Brunner, H., Boller, T., Coutinho, D., et al. 2018, in *Society of Photo-Optical Instrumentation Engineers (SPIE) Conference Series*, Vol. 10699, *Space Telescopes and Instrumentation 2018: Ultraviolet to Gamma Ray*, ed. J.-W. A. den Herder, S. Nikzad, & K. Nakazawa, 106995G
- Brunner, H., Liu, T., Lamer, G., et al. 2022, *A&A*, 661, A1
- Bunner, A. N., Coleman, P. L., Kraushaar, W. L., McCammon, D., & Williamson, F. O. 1973, *ApJ*, 179, 781
- Camilloni, F. & Becker, W. 2023, arXiv e-prints, arXiv:2310.03426
- Cash, W. 1979, *ApJ*, 228, 939
- Clark, S. E. & Hensley, B. S. 2019, *ApJ*, 887, 136
- Collischon, C., Sasaki, M., Mecke, K., Points, S. D., & Klatt, M. A. 2021, *A&A*, 653, A16
- Cumbee, R. S., Mullen, P. D., Lyons, D., et al. 2018, *ApJ*, 852, 7
- Dennison, B., Simonetti, J. H., & Topasna, G. A. 1998, *PASA*, 15, 147
- Elwood, B. D., Murphy, J. W., & Diaz, M. 2017, arXiv e-prints, arXiv:1701.07057
- Finkbeiner, D. P. 2003, *ApJS*, 146, 407
- Foster, A., Cui, X., Dupont, M., Smith, R., & Brickhouse, N. 2020, in *American Astronomical Society Meeting Abstracts*, Vol. 235, *American Astronomical Society Meeting Abstracts #235*, 180.01
- Fukugita, M. & Peebles, P. J. E. 2006, *ApJ*, 639, 590
- Gao, X. Y., Han, J. L., Reich, W., et al. 2011, *A&A*, 529, A159
- Gaustad, J. E., McCullough, P. R., Rosing, W., & Van Buren, D. 2001, *PASP*, 113, 1326
- Giampapa, M. S., Rosner, R., Kashyap, V., et al. 1996, *ApJ*, 463, 707
- Gilli, R., Comastri, A., & Hasinger, G. 2007, *A&A*, 463, 79
- Graham, D. A., Haslam, C. G. T., Salter, C. J., & Wilson, W. E. 1982, *A&A*, 109, 145
- Green, D. A. 2019, *Journal of Astrophysics and Astronomy*, 40, 36
- Gupta, A., Kingsbury, J., Mathur, S., et al. 2021, *ApJ*, 909, 164
- Hamilton, A. J. S., Sarazin, C. L., & Chevalier, R. A. 1983, *ApJS*, 51, 115
- Harris, C. R., Millman, K. J., van der Walt, S. J., et al. 2020, *Nature*, 585, 357
- HI4PI Collaboration, Ben Bekhti, N., Flöer, L., et al. 2016, *A&A*, 594, A116
- Hunter, J. D. 2007, *Computing In Science & Engineering*, 9, 90
- Kaastra, J. S. 2017, *A&A*, 605, A51
- Kavanagh, P. J., Sasaki, M., Filipović, M. D., et al. 2022, *MNRAS*, 515, 4099
- Kim, I. J., Min, K. W., Seon, K. I., et al. 2007, *ApJ*, 665, L139
- Knies, J. R. 2022, Phd thesis, Friedrich-Alexander-Universität Erlangen-Nürnberg (FAU)
- Knies, J. R., Sasaki, M., Fukui, Y., et al. 2021, *A&A*, 648, A90
- Knies, J. R., Sasaki, M., & Plucinsky, P. P. 2018, *MNRAS*, 477, 4414
- Kuntz, K. D. & Snowden, S. L. 2000, *ApJ*, 543, 195
- Lallement, R., Vergely, J. L., Babusiaux, C., & Cox, N. L. J. 2022, *A&A*, 661, A147
- Leahy, D. A. 1986, *A&A*, 156, 191
- Leahy, D. A., Naranan, S., & Singh, K. P. 1985, *MNRAS*, 213, 15P
- Leahy, D. A., Naranan, S., & Singh, K. P. 1986, *MNRAS*, 220, 501
- Leahy, D. A., Williams, J., & Lawton, B. 2017, *SNRPy: Supernova remnant evolution modeling*, *Astrophysics Source Code Library*, record ascl:1703.006
- Liu, W., Chiao, M., Collier, M. R., et al. 2017, *ApJ*, 834, 33
- Locatelli, N., Ponti, G., Zheng, X., et al. 2023, arXiv e-prints, arXiv:2310.10715
- McMillan, P. J. 2017, *MNRAS*, 465, 76
- Merloni et al. 2023, *A&A*, accepted
- Müller, B., Heger, A., Liptai, D., & Cameron, J. B. 2016, *MNRAS*, 460, 742
- Nousek, J. A., Cowie, L. L., Hu, E., Lindblad, C. J., & Garmire, G. P. 1981, *ApJ*, 248, 152
- Planck Collaboration, Aghanim, N., Akrami, Y., et al. 2020, *A&A*, 641, A1
- Plucinsky, P. P., Snowden, S. L., Aschenbach, B., et al. 1996, *ApJ*, 463, 224
- Ponti, G., Zheng, X., Locatelli, N., et al. 2022, arXiv e-prints, arXiv:2210.03133
- Predehl, P., Andritschke, R., Arefiev, V., et al. 2021, *A&A*, 647, A1
- Ranasinghe, S. & Leahy, D. 2022, *ApJ*, 940, 63
- Reynolds, R. J., Haffner, L. M., & Madsen, G. J. 2002, in *Astronomical Society of the Pacific Conference Series*, Vol. 282, *Galaxies: the Third Dimension*, ed. M. Rosada, L. Binette, & L. Arias, 31
- Reynolds, S. P. 2017, in *Handbook of Supernovae*, ed. A. W. Alsabti & P. Murdin, 1981
- Sanders, J. S. 2006, *MNRAS*, 371, 829
- Sanders, J. S., Fabian, A. C., Taylor, G. B., et al. 2016, *MNRAS*, 457, 82
- Sasaki, M., Knies, J., Haberl, F., et al. 2022, *A&A*, 661, A37
- Smith, R. K., Brickhouse, N. S., Liedahl, D. A., & Raymond, J. C. 2001, *ApJ*, 556, L91
- Smith, R. K., Foster, A. R., & Brickhouse, N. S. 2012, *Astronomische Nachrichten*, 333, 301
- Snowden, S. L., Mushotzky, R. F., Kuntz, K. D., & Davis, D. S. 2008, *A&A*, 478, 615
- Taylor, G. 1950, *Proceedings of the Royal Society of London Series A*, 201, 159
- Thorsett, S. E., Benjamin, R. A., Brisken, W. F., Golden, A., & Goss, W. M. 2003, *ApJ*, 592, L71
- Truelove, J. K. & McKee, C. F. 1999, *ApJS*, 120, 299
- Vergely, J. L., Lallement, R., & Cox, N. L. J. 2022, *A&A*, 664, A174
- Vuong, M. H., Montmerle, T., Grosso, N., et al. 2003, *A&A*, 408, 581
- Weinberger, R., Temporal, S., & Stecklum, B. 2006, *A&A*, 448, 1095
- Welsh, B. Y., Sfeir, D. M., Sallmen, S., & Lallement, R. 2001, *A&A*, 372, 516
- White, R. L. & Long, K. S. 1991, *ApJ*, 373, 543
- Wilms, J., Allen, A., & McCray, R. 2000, *ApJ*, 542, 914
- Wulf, D., Eckart, M. E., Galeazzi, M., et al. 2019, *ApJ*, 884, 120
- Xiang, Y. & Jiang, Z. 2021, arXiv e-prints, arXiv:2104.10842
- Xiao, L. & Zhu, M. 2012, *A&A*, 545, A86
- Yeung, M. C. H., Freyberg, M. J., Ponti, G., et al. 2023, arXiv e-prints, arXiv:2306.05858
- Yoshino, T., Mitsuda, K., Yamasaki, N. Y., et al. 2009, *PASJ*, 61, 805
- Zhang, Y., Sun, T., Wang, C., et al. 2022, *ApJ*, 932, L1
- Zharikov, S., Zyuzin, D., Shibano, Y., et al. 2021, *MNRAS*, 502, 2005

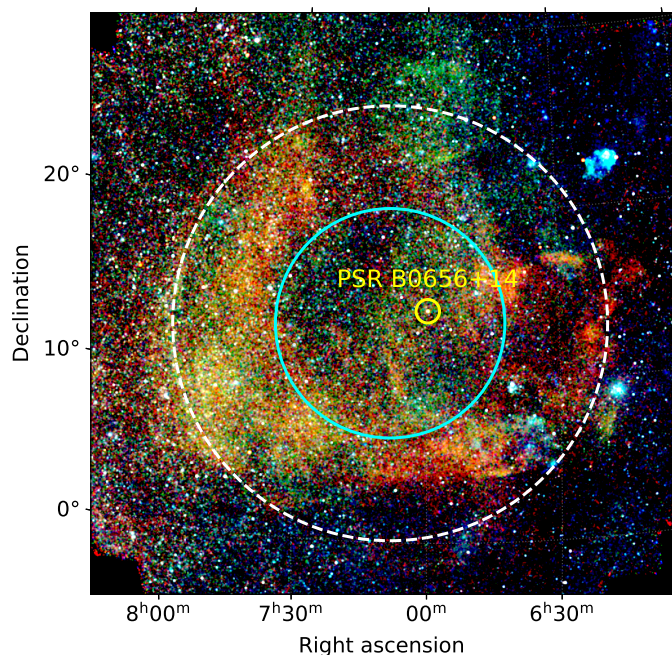


Fig. A.1: eROSITA X-ray mosaic as in Fig. 1, with the estimated shell extent of the Monogem Ring SNR (white dashed) if assuming a single structure at $D = 300$ pc. The cyan circle highlights the darker interior of the remnant which was excluded for estimating the SNR properties, therefore only using the limb-brightened shell in an annulus. The current position of PSR B0656+14 is shown in yellow.

Appendix A: Alternative geometry with a single SNR for the Monogem Ring

Appendix B: Alternative CGM Model

From the results of background analysis with “Model B”, we obtained normalizations of about one order of magnitude higher near the disk for the CGM component. While a certain increase in flux towards the disk is expected for a Galactic component, such a strong increase might hint towards inaccuracies in the underlying assumptions of the model. One possible explanation could be, that the high column density measured in the HI4PI (HI4PI Collaboration et al. 2016) towards the Galactic disk only partially affects the CGM component.

Since the exact nature of both the CGM and hot corona are not yet fully understood, we therefore introduced individual absorption models (TBABS) to both components. They were let free to fit, with the upper bound fixed to the HI4PI, since it should be impossible to obtain a stronger absorption. Using this modified model, the absorption for the hot corona was almost exclusively fit with the HI4PI value, while the CGM was fit with significantly lower absorption compared to the HI4PI values in the disk ($b \pm 10^\circ$). Therefore, we adopted the full absorption value reported from the HI4PI survey for both the hot corona and CXB, using a single TBABS like before, and a separate TBABS component for the CGM. In the following fits, we initially set the CGM absorption component to half of the HI4PI value, with an upper bound equal to the HI4PI value.

In addition, the modification to the CGM caused the ACX2 component normalizations to be consistent with zero for most regions. While the other model component at lower energies - the LHB component - appears to remain the same between the

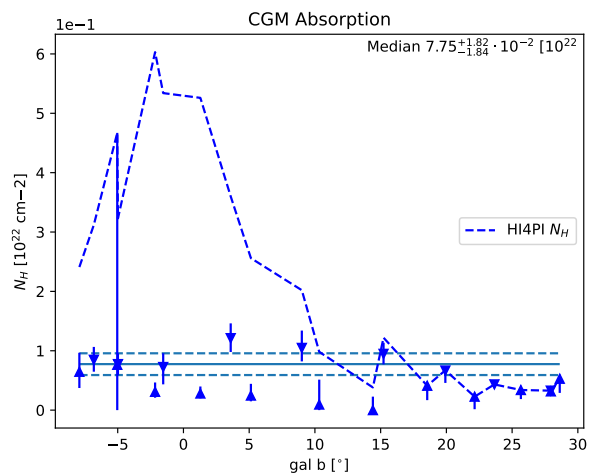


Fig. B.1: The CGM specific foreground absorption if we decouple the absorption component from the Galactic N_{H} absorption. The solid lines show the median, while the dashed lines show the upper/lower limit median (90% CI).

different models, there appears to be a degeneracy between the ACX2 model and the CGM component, if we assume it to be only weakly absorbed. Due to enhanced solar activities during eRASS 3 and 4, we expect at least a moderate amount of contamination by SWCX in the combined eRASS:4 data. Therefore, we continue our analysis with “Model B” instead of this alternative model.

Appendix C: Spectral fitting routine for source regions

The detailed fitting routine of the source regions, both for the manual regions and contour-bins, was performed as follows. Similar to the background, we fitted the FWC normalization constants from the hard-energy tail of the spectrum, before modeling the spectrum in the energy range $0.2 - 3.0$ keV. The column density of the background TBABS component was fixed to the HI4PI survey value (HI4PI Collaboration et al. 2016). Initial values for the NEI component were chosen as $kT = 0.25$ keV, fixed solar abundance, the ionization timescale $\tau = 1 \cdot 10^{11}$ s cm^{-3} and normalization of $\eta = 1 \cdot 10^{-7}$ cm^{-5} arcmin^{-2} . We also used the cstat fit statistic for the source regions. If the threshold of $\text{cstat}/\text{d.o.f.} > 1.14$ was exceeded after the initial fit, we increased the background parameter uncertainties by 10% and repeated the fit. In a last step, we checked the source component parameters for unrealistically high or low values and reset the respective parameters before performing another fit.

After the final fit, we calculated the uncertainties of the free-to-fit source component parameters. In order to reduce the computation time due to unnecessary free parameters, we froze the normalization constants for the FWC and TM calibration, since they are in any case constrained to a very narrow range. We first attempted to calculate the uncertainties by using the ERROR command for each parameter. If the diagnostic error string indicated problems, we instead calculated the uncertainties with the STEPPAR command in an iterative automatic way. The initial STEPPAR calculation was performed in an interval (90% – 110%) of the best-fit value, using 20 steps. If no appropriate 90% confidence interval limit was found, the calculation range was increased in the respective - or both - direction(s). This procedure was repeated up to a maximum of ten times. For the τ and TBABS N_{H} parameters,

the relative change was chosen higher. Additionally, for τ and N_{H} , the error was calculated with a logarithmic grid. We used this approach for both the contour-bins and the manually defined large regions.

In addition, because we have higher statistics in the manually defined regions, we systematically tested SNR-characteristic elemental abundances. After the final fit with solar abundances, we tested the following elements: O, Ne, Mg, Si, S, and Fe. The elements were fitted simultaneously. Next, we checked for unrealistically low or high values, and reset those elements back to solar abundances. Then, we performed another fit. Those two steps were repeated until all elements that were free to fit had realistic values. We confirmed if the free-to-fit abundances improved the model above the 3σ significance level, using the `FTEST` command, and if not, reset the model to solar values. Again, we calculated the uncertainties as described above.

Appendix D: Comparison of methods

In order to assess our spectral analysis methods, we made a direct comparison of the fit results using the same model with both methods, which are contour-binning and manually defining the regions. The comparison is shown in Fig. D.1. The fit results of the two methods appear to agree remarkably well, independent of the spectral model we used. This comparison also highlights the strengths and weaknesses of both methods. The contour binning allows to determine a distribution of plasma parameters while at the same time the individual uncertainties are higher. Contrary, the manually defined regions basically average over a range of plasma conditions which is demonstrated by the fit result often being located right in the middle of the distribution of plasma parameters we derived with the contour-binning. At the same time, the uncertainties are smaller, however, under the assumption that we only have a singular plasma (or plasma state) which is clearly not the case. Using both analysis methods, we are able to mitigate the weaknesses of both methods and we obtain a much more complete picture about the plasma in our sources.

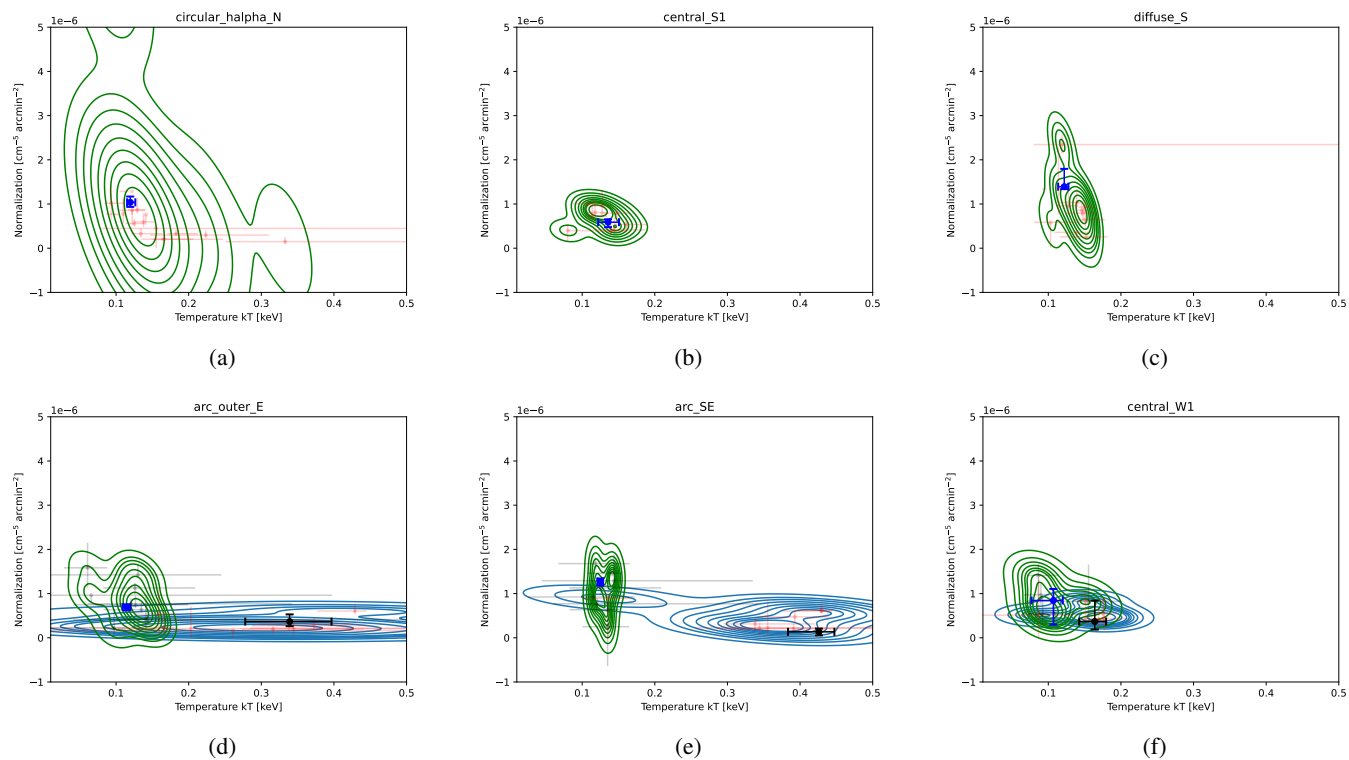


Fig. D.1: Comparison between the contour-bin and manually defined region spectral fits. The contours show the density of the fit values from the contour-bins, weighted by the area overlap with the respective manual region. In (a)-(c) we show examples using the simple $\text{TBABS} \times \text{NEI}$ model. The green contours and red markers show the best fit values with uncertainties of the contour-bins. The fit result from the manually defined region is shown with a blue marker. In (d)-(f) we show the $\text{TBABS} \times \text{VAPEC}_1 + \text{APEC}_2$ model, where the green contours and black markers show the low temperature APEC, and the blue contours and red markers the hotter VAPEC component best fit values. The fit results from the manually defined region are shown with a blue and black marker.